

VQC-MLPNet: An Unconventional Hybrid Quantum-Classical Architecture for Scalable and Robust Quantum Machine Learning

Jun Qi¹, Chao-Han Yang², Pin-Yu Chen³, Min-Hsiu Hsieh⁴

1. School of Electrical and Computer Engineering, Georgia Institute of Technology, Atlanta, GA 30332, USA

2. NVIDIA Research, Santa Clara, CA 95051, USA

3. IBM Thomas J. Watson Research Center, NY, 10598, USA

4. Hon Hai (Foxconn) Quantum Computing Research Center, Taipei, 114, Taiwan

E-mail: jqi41@gatech.edu, pin-yu.chen@ibm.com, minhsiuh@gmail.com

Abstract. Variational Quantum Circuits (VQCs) offer a novel pathway for quantum machine learning, yet their practical application is hindered by inherent limitations such as constrained linear expressivity, optimization challenges, and acute sensitivity to quantum hardware noise. This work introduces VQC-MLPNet, a scalable and robust hybrid quantum-classical architecture designed to overcome these obstacles. By innovatively employing quantum circuits to dynamically generate parameters for classical Multi-Layer Perceptrons (MLPs) via amplitude encoding and parameterized quantum operations, VQC-MLPNet substantially expands representation capabilities and augments training stability. We provide rigorous theoretical guarantees via statistical learning techniques and Neural Tangent Kernel analysis, explicitly deriving upper bounds on approximation, uniform deviation, and optimization errors. These theoretical insights demonstrate exponential improvements in representation capacity relative to quantum circuit depth and the number of qubits, providing clear computational advantages over standalone quantum circuits and existing hybrid quantum architectures. Our theoretical claims are empirically corroborated through extensive experiments, including classifying semiconductor quantum-dot charge states and predicting genomic transcription factor binding sites, demonstrating resilient performance even under realistic IBM quantum noise simulations. This research establishes a theoretically sound and practically robust framework, advancing the frontiers of quantum-enhanced learning for unconventional computing paradigms in the Noisy Intermediate-Scale Quantum era and beyond.

1. Introduction

Quantum computing has emerged as a promising paradigm capable of solving complex computational problems beyond the reach of classical systems [1, 2]. In the Noisy Intermediate-Scale Quantum (NISQ) era, characterized by quantum hardware

constraints such as noise, decoherence, and limited qubit count [3, 4], hybrid quantum-classical architectures have gained significant attention as practical pathways for leveraging quantum advantages in machine learning applications [5–8]. Among the core quantum components used in such frameworks, Variational Quantum Circuits (VQCs) have become a foundational approach in quantum machine learning [7, 9–12]. VQCs are parameterized quantum models trained via classical optimization loops and are often regarded as quantum analogs of neural networks due to their layered gate structures and tunable parameters [8, 13, 14]. Nevertheless, VQCs encounter critical challenges, including limited representation capacity stemming from their inherent linearity [15], difficulties with scalable data encoding [16–18], optimization problems arising from a non-convex training landscape [19–21], and the well-known barren plateau phenomenon [19, 22].

This work proposes VQC-MLPNet, a hybrid quantum-classical neural network architecture that integrates a Variational Quantum Circuit (VQC) with a classical Multi-Layer Perceptron (MLP) [23] to overcome these fundamental limitations. Specifically, our proposed architecture employs a VQC to generate a subset of the MLP’s weight parameters, effectively combining quantum-enhanced feature embeddings with the classical neural network’s nonlinear expressivity. This architectural synergy substantially boosts representation power, generalization performance, and optimization stability compared to traditional VQCs. Importantly, VQC-MLPNet maintains computational scalability and practical feasibility for near-term quantum devices by operating classically during inference, making it especially suitable for deployment on current quantum hardware.

Recent hybrid quantum-classical models, such as TTN-VQC [24, 25], have successfully demonstrated improved expressivity by integrating classical tensor-train networks with variational quantum classifiers. The TTN-VQC architecture addresses common challenges and limitations typical of hybrid quantum-classical designs, thereby establishing itself as a representative and widely adopted baseline among existing hybrid quantum-classical models [24, 26]. Nonetheless, like other prior hybrid models such as Quantum Convolutional Neural Networks (QCNN) [10] and Quantum Transformers [27, 28], TTN-VQC suffers from key limitations, including high complexity and resource demands due to extensive qubit usage, persistent optimization challenges, and inherent linearity of quantum circuits, which limits generalization on complex datasets. In contrast, VQC-MLPNet offers a practical and efficient alternative, addressing these drawbacks by incorporating classical nonlinearities, improving optimization landscapes, and reducing resource demands, thereby enhancing expressivity and trainability.

To rigorously assess the effectiveness of VQC-MLPNet, we perform a structured theoretical framework of risk decomposition [29, 30] that systematically factorizes the total learning error into three key contributing components: approximation error, uniform deviation, and optimization error. As illustrated in Figure 2, given a target operator h^* , we aim to identify the optimal parametric VQC-MLPNet operator f_{θ^*} within the VQC-MLPNet functional space \mathcal{F}_{vm} , where θ represents the VQC-MLPNet

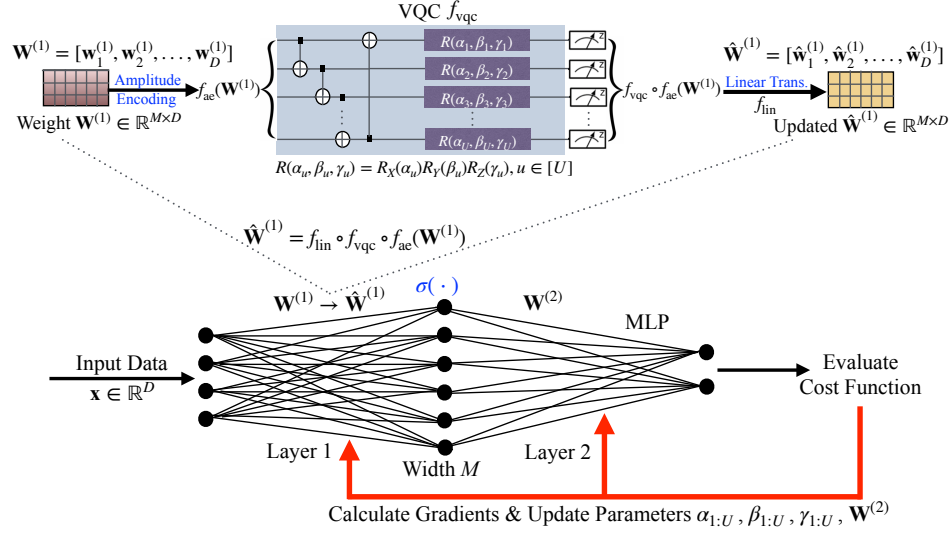


Figure 1. An Illustration of the VQC-MLPNet structure. The VQC-MLPNet architecture is a hybrid quantum-classical neural network where the VQC generates the MLP parameters $\hat{\mathbf{W}}^{(1)}$ for its first hidden layer. During training, the VQC uses amplitude encoding to encode $\mathbf{W}^{(1)}$. The transformed parameters $\{\alpha_{1:U}, \beta_{1:U}, \gamma_{1:U}\}$ in f_{vqc} are updated through quantum operations before being integrated into the first hidden layer of the MLP. Once trained, the VQC is no longer needed for inference, making the model scalable for deployment.

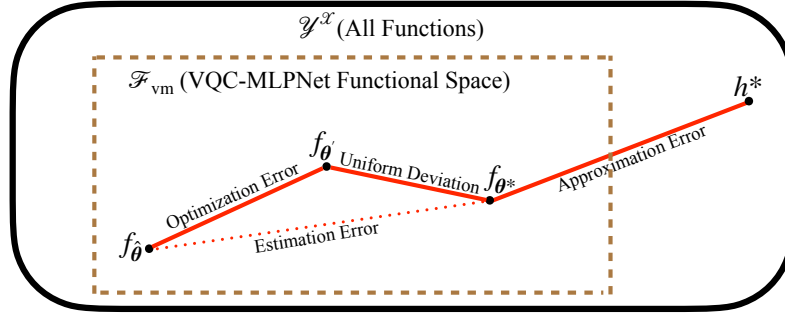


Figure 2. The error performance analysis of VQC-MLPNet illustrates the decomposition of total learning error into three key components. Given a target function h^* , the optimal VQC-MLPNet introduces an approximation error relative to h^* . The empirical risk minimizer f_{θ^*} , obtained from training data, results in a uniform deviation from f_{θ^*} . Finally, the algorithmically returned operator $f_{\hat{\theta}}$, derived through gradient-based optimization, incurs an optimization error concerning f_{θ^*} .

parameters in the VQC-MLPNet parameter space.

The deviation between h^* and f_{θ^*} defines the approximation error, which quantifies the model's ability to represent the target function. In practice, empirical risk minimization is performed on the training data, yielding an empirical risk minimizer $f_{\theta'}$, leading to uniform deviation, which is the discrepancy between $f_{\theta'}$ and f_{θ^*} . Furthermore, the final VQC-MLPNet operator $f_{\hat{\theta}}$ is obtained using a gradient-based optimization algorithm, introducing an optimization error that measures the difference between $f_{\hat{\theta}}$

Table 1. Summarizing our theoretical results of VQC-MLPNet and comparing them with MLP and TTN-VQC.

Error Component	VQC-MLPNet	MLP	TTN-VQC [24]
Approximation Error	$\frac{C_1}{\sqrt{M}} + C_2 e^{-\alpha L} + \frac{C_3}{2^{\beta U}}$	$\frac{C}{\sqrt{M}}$	$\frac{C_1}{\sqrt{M}} + \frac{C_2}{\sqrt{L}}$
Uniform Deviation	$\frac{2\Lambda\sqrt{L}r}{\sqrt{ S }}$	$\frac{2\Lambda\Lambda' r}{\sqrt{ S }}$	$\frac{2r}{\sqrt{ S }} \left(\sqrt{\sum_{j=1}^J \Lambda_j^2} + \Lambda' \right)$
Optimization Condition	NTK	Over-Param. + NTK	μ -PL condition
Optimization Error	$C_0 e^{-\lambda_{\min}(\mathcal{K}_{\text{vm}})t}$	$C_0 e^{-\lambda_{\min}(\mathcal{K}_{\text{mlp}})t}$	$\epsilon_{\text{opt}}(0) e^{-\mu t}$

and f_{θ^*} . Moreover, the uniform deviation and optimization error sum constitute the estimation error, representing the discrepancy between the learned model $f_{\hat{\theta}}$ and the best achievable operator f_{θ^*} .

Mathematically, the framework of risk decomposition considers the excess risk of $f_{\hat{\theta}}$ as $\mathcal{R}(f_{\hat{\theta}}) - \mathcal{R}(h^*)$, which can be decomposed as the sum of approximation error and estimation error as shown below:

$$\mathcal{R}(f_{\hat{\theta}}) - \mathcal{R}(h^*) = \underbrace{\{\mathcal{R}(f_{\theta^*}) - \mathcal{R}(h^*)\}}_{\text{Approximation Error}} + \underbrace{\{\mathcal{R}(f_{\hat{\theta}}) - \mathcal{R}(f_{\theta^*})\}}_{\text{Estimation Error}}, \quad (1)$$

where we separately define $\mathcal{R}(\cdot)$ and $\hat{\mathcal{R}}(\cdot)$ as expected risk and empirical risk, and the estimation error $\mathcal{R}(f_{\hat{\theta}}) - \mathcal{R}(f_{\theta^*})$ can be further decomposed as:

$$\begin{aligned} \mathcal{R}(f_{\hat{\theta}}) - \mathcal{R}(f_{\theta^*}) &= \{\mathcal{R}(f_{\hat{\theta}}) - \hat{\mathcal{R}}(f_{\hat{\theta}})\} + \{\hat{\mathcal{R}}(f_{\theta'}') - \mathcal{R}(f_{\theta'}')\} + \{\hat{\mathcal{R}}(f_{\hat{\theta}}) - \hat{\mathcal{R}}(f_{\theta'}')\} \\ &\leq \underbrace{2 \sup_{\theta \in \Theta} |\hat{\mathcal{R}}(f_{\theta}) - \mathcal{R}(f_{\theta})|}_{\text{Uniform Deviation}} + \underbrace{\sup_{\hat{\theta} \in \Theta} (\hat{\mathcal{R}}(f_{\hat{\theta}}) - \hat{\mathcal{R}}(f_{\theta'}'))}_{\text{Optimization Error}}. \end{aligned} \quad (2)$$

We aim to provide upper bounds on each error component to highlight VQC-MLPNet's representation and generalization powers, where the approximation error is related to the representation power, and the estimation error (the sum of uniform deviation and optimization error) corresponds to the generalization capability. This work focuses on the classification tasks, and accordingly, we assume both $\mathcal{R}(\cdot)$ and $\hat{\mathcal{R}}(\cdot)$ as the cross-entropy loss function. The related theoretical results are shown in Table 1 and summarized below:

- **Approximation Error:** VQC-MLPNet achieves significantly improved representation power due to its exponential reduction of approximation error concerning quantum circuit depth (L) and the number of qubits (U). With the over-parameterization setting for MLP, the MLP's hidden-layer width (M) is significantly large so that the term $\frac{C_1}{\sqrt{M}}$ is very close to 0. Thus, the VQC-MLPNet bound scales as $C_2 e^{-\alpha L} + \frac{C_3}{2^{\beta U}}$, demonstrating exponential expressivity advantages over TTN-VQC, which scales polynomially as $\frac{C_1}{\sqrt{M}} + \frac{C_2}{\sqrt{L}}$. Since classical MLP, which only scales as $\frac{C}{\sqrt{M}}$, VQC-MLPNet exhibits similar representation capability to MLP.

- **Estimation Error (Uniform Deviation + Optimization Error):** For the uniform deviation components, VQC-MLPNet exhibits a better-conditioned $\frac{2\Delta\sqrt{L}r}{\sqrt{|S|}}$, outperforming TTN-VQC and classical MLP by effectively controlling model complexity through the circuit depth (L). Additionally, the optimization error analysis leveraging the Neural Tangent Kernel (NTK) theory [31–33] shows that VQC-MLPNet provides favorable training stability and exponential convergence, avoiding the stringent μ -Polyak-Łojasiewicz (μ -PL) condition [34, 35] required by TTN-VQC. In contrast, classical MLP optimization conditions rely heavily on over-parameterization combined with the NTK theory, potentially requiring significantly more parameters.

By providing explicit upper bounds on each error component, we demonstrate the theoretical superiority of VQC-MLPNet over standalone VQCs and other hybrid architectures, such as TTN-VQC. We explicitly evaluate our model under realistic IBM quantum noise conditions, including amplitude and phase damping rates [36], demonstrating substantial robustness and generalization resilience in the NISQ era. Our empirical validation spans highly interdisciplinary scientific applications: (1) semiconductor quantum-dot charge-state classification [37, 38], which supports quantum device calibration and optimization relevant to quantum computing hardware, and (2) genome transcription factor binding-site prediction [39], an essential task in computational biology and genomics. Furthermore, our method inherently generalizes to other scientific domains such as quantum chemistry and computational materials science, where scalable, accurate quantum-enhanced machine learning can significantly accelerate discovery and innovation.

2. Results

2.1. VQC-MLPNet Framework

Figure 2 illustrates our proposed VQC-MLPNet architecture, a hybrid quantum-classical neural network integrating a VQC into the classical MLP pipeline. The VQC generates a subset of the MLP’s weight parameters, effectively embedding quantum-enhanced features into a classical neural structure. During training, the classical weight $\mathbf{W}^{(1)}$ from the MLP is first encoded into quantum states through amplitude encoding. Formally, each weight vector $\mathbf{w}_d^{(1)} \in \mathbb{R}^M$, extracted from the weight matrix $\mathbf{W}^{(1)} = [\mathbf{w}_1^{(1)}, \mathbf{w}_2^{(1)}, \dots, \mathbf{w}_D^{(1)}]^\top \in \mathbb{R}^{M \times D}$, is transformed into a quantum state:

$$|\mathbf{w}_d^{(1)}\rangle = \frac{1}{\|\mathbf{w}_d^{(1)}\|_2} \sum_{m=0}^{M-1} \mathbf{w}_d^{(1)}(m) |m\rangle, \quad (3)$$

where M is the MLP hidden layer width and the required number of qubits U satisfies $2^U \geq M$.

Subsequently, these quantum states are processed through the VQC operator f_{vqc} , yielding a quantum-enhanced weight matrix $\hat{\mathbf{W}}^{(1)}$. A linear operator f_{lin} can optionally

be applied, aligning the VQC output dimensions to match $\mathbf{W}^{(1)}$:

$$\hat{\mathbf{W}}^{(1)} = f_{\text{lin}} \circ f_{\text{vqc}} \circ f_{\text{ae}}(\mathbf{W}^{(1)}). \quad (4)$$

The quantum-enhanced weight $\hat{\mathbf{W}}^{(1)}$ then passes through a nonlinear activation function $\sigma(\cdot)$, such as ReLU, followed by another classical linear transformation parameterized by $\mathbf{W}^{(2)}$, producing the final output. The proposed VQC-MLPNet architecture simultaneously leverages quantum expressivity and classical representation power by combining quantum-generated parameters with classical nonlinearities. Notably, the architecture maintains classical computational scalability during inference, as quantum computations are only necessary for the training phase.

From an optimization perspective, VQC-MLPNet contains tunable parameters $\alpha_{1:U}$, $\beta_{1:U}$ and $\gamma_{1:U}$ (associated with quantum rotation gates $R_X(\cdot)$, $R_Y(\cdot)$ and $R_Z(\cdot)$), alongside the classical parameter $\mathbf{W}^{(2)}$. These parameters are updated iteratively via gradient-based optimization during training. At inference, the model operates entirely classically by utilizing the fixed quantum-generated weight matrix $\hat{\mathbf{W}}^{(1)}$, thereby eliminating the need for quantum processing during deployment.

The VQC-MLPNet architecture is specifically designed to bridge the gap between purely quantum and purely classical models. By enabling the VQC to influence the MLP weight space, the model benefits from quantum-enhanced transformations without entirely relying on quantum computation during inference. As a result, VQC-MLPNet achieves a balanced integration of quantum expressivity and classical trainability, making it highly suitable for practical quantum-enhanced machine learning in the current NISQ era.

2.2. Error Performance Analysis

To rigorously evaluate VQC-MLPNet, we perform a comprehensive theoretical analysis that decomposes the total learning error into three key components: approximation error, uniform deviation, and optimization error. We derive upper bounds for each error type and systematically demonstrate how VQC-MLPNet outperforms standalone MLPs and traditional hybrid architectures, such as TTN-VQC, in terms of expressivity, generalization capability, and trainability.

• Mathematical Preliminaries:

We define the VQC-MLPNet's parameters as the vector $\boldsymbol{\theta} = \boldsymbol{\theta}_{\text{vqc}} \oplus \boldsymbol{\theta}_{W^{(2)}}$, where the VQC's parameter $\boldsymbol{\theta}_{\text{vqc}} = [\alpha_{1:U} \ \beta_{1:U} \ \gamma_{1:U}]^\top$ and $\boldsymbol{\theta}_{W^{(2)}} = [\text{vec}(\mathbf{W}^{(2)})]^\top$. Then, given two constant constraints Λ_Q and Λ , we denote the VQC-MLPNet's functional space as \mathcal{F}_{vm} with its parameter sapce Θ as:

$$\Theta = \{\boldsymbol{\theta} = \boldsymbol{\theta}_{\text{vqc}} \oplus \boldsymbol{\theta}_{W^{(2)}} \mid \|\boldsymbol{\theta}_{\text{vqc}}\|_2 \leq \Lambda_Q, \|\boldsymbol{\theta}_{W^{(2)}}\|_2 \leq \Lambda\}. \quad (5)$$

Moreover, we assume the parameterized VQC-MLPNet operator $f_{\boldsymbol{\theta}}$ for its parameters $\boldsymbol{\theta} \in \Theta$. In particular, we separately define $\boldsymbol{\theta}^*$ and $\boldsymbol{\theta}'$ as:

$$\boldsymbol{\theta}^* := \arg \inf_{\boldsymbol{\theta} \in \Theta} \mathcal{R}(f_{\boldsymbol{\theta}}) \quad \text{and} \quad \boldsymbol{\theta}' := \arg \inf_{\boldsymbol{\theta} \in \Theta} \hat{\mathcal{R}}(f_{\boldsymbol{\theta}}), \quad (6)$$

where $\mathcal{R}(\cdot)$ and $\hat{\mathcal{R}}(\cdot)$ refer to the expected risk and empirical risk, respectively. $\boldsymbol{\theta}^*$ and $\boldsymbol{\theta}'$ separately denote the optimal VQC-MLPNet operator and the related empirical risk minimizer.

- **Approximation Error:**

The approximation error quantifies the discrepancy between the target operator h^* and the best achievable approximation $f_{\boldsymbol{\theta}^*}$ within the VQC-MLPNet hypothesis space, as formally established in Theorem 1.

Theorem 1 (Approximation Error Bound) *Given a target operator h^* , let $f_{\boldsymbol{\theta}^*}$ denote the optimal VQC-MLPNet operator within the hypothesis class. Then, the approximation error ϵ_{app} satisfies the following upper bound:*

$$\epsilon_{\text{app}} = \mathcal{R}(f_{\boldsymbol{\theta}^*}) - \mathcal{R}(h^*) \leq \frac{C_1}{\sqrt{M}} + C_2 e^{-\alpha L} + \frac{C_3}{2^{\beta U}}, \quad (7)$$

where M is the width of the MLP's hidden layer, L is the depth of the VQC, and U denotes the number of qubits. Constants $C_1, C_2, C_3, \alpha > 0$ are problem-dependent, and $0 < \beta \leq \frac{1}{2}$ reflects a scaling penalty associated with amplitude encoding.

Theorem 1 highlights that in an over-parameterized scenario (large width M) [40], the approximation error predominantly depends on the VQC structure. Thus, VQC-MLPNet attains a substantially tighter error bound than TTN-VQC, owing to the exponential expressivity improvements by increasing quantum circuit depth L and qubit count U .

Theoretically, increasing U and L significantly enhances approximation power. However, setting large values of these parameters may be challenging. To address this, we provide a guideline in Proposition 1 for choosing a moderate circuit depth L to meet a specified error threshold.

Proposition 1 (Moderate-depth Circuit Selection) *For the expressive error term $C_2 e^{-\alpha L}$, given a constant $\tau > 0$, a logarithmic VQC's depth $L \sim \mathcal{O}(\log(1/\tau))$ suffices to ensure an error remains below τ .*

- **Uniform Deviation:**

This uniform deviation captures the generalization error, representing the difference between the empirical risk minimizer $f_{\boldsymbol{\theta}'}$ obtained from training data and the optimal $f_{\boldsymbol{\theta}^*}$, as formulated in Theorem 2.

Theorem 2 (Uniform Deviation Bound) *VQC-MLPNet achieves a favorable bound on uniform deviation due to the controlled complexity of its hybrid architecture:*

$$\epsilon_{\text{dev}} = 2 \sup_{\boldsymbol{\theta} \in \Theta} \left| \hat{\mathcal{R}}(f_{\boldsymbol{\theta}}) - \mathcal{R}(f_{\boldsymbol{\theta}}) \right| \leq \frac{2\Lambda\Lambda_Q r}{\sqrt{|S|}}, \quad \text{s.t., } \|\boldsymbol{\theta}_{W(2)}\|_2 \leq \Lambda, \|\boldsymbol{\theta}_{\text{vqc}}\|_2 \leq \Lambda_Q, \quad (8)$$

where Λ and Λ_Q are model norm constraints, r is the input data norm bound, and $|S|$ is the number of training samples.

Theorem 2 implies that deeper circuits improve expressivity but could increase model complexity and potential generalization challenges. Furthermore, motivated by the statistical behavior of random quantum circuits, where feature norms typically scale as the square root of depth [2, 9, 11], we assume $\Lambda_Q = \mathcal{O}(\sqrt{L})$. This moderate scaling ensures that the circuit depth enhances model expressivity without excessively inflating the uniform deviation term, supporting both approximation and generalization properties of the VQC-MLPNet architecture. Thus, we refine our uniform deviation bound in Proposition 2:

Proposition 2 (Refined Uniform Deviation Bound) *Given constraints on the VQC-MLPNet parameters and VQC depth of \sqrt{L} , the refined uniform deviation bound is:*

$$\epsilon_{\text{dev}} \leq \frac{2\Lambda\sqrt{L}r}{|S|}. \quad (9)$$

- **Optimization Error:**

To analyze the effectiveness of gradient-based training in VQC-MLPNet, we leverage the Neural Tangent Kernel (NTK) theory. The NTK theory describes how the neural network behaves during training by observing how small parameter changes affect predictions. Unlike TTN-VQC, which relies on strong optimization assumptions such as the Polyak-Łojasiewicz (PL) condition [34, 35], VQC-MLPNet naturally ensures exponential convergence due to its well-conditioned NTK and its smallest eigenvalue being not too small, as shown in Eq. (10).

$$\epsilon_{\text{opt}}(t) = \sup_{\hat{\boldsymbol{\theta}} \in \Theta} \left(\hat{\mathcal{R}}(f_{\hat{\boldsymbol{\theta}}}) - \hat{\mathcal{R}}(f_{\boldsymbol{\theta}^*}) \right) \leq C_0 e^{-\lambda_{\min}(\mathcal{K}_{\text{vm}})t}, \quad (10)$$

where C_0 is a constant related to first-order gradients of $f_{\boldsymbol{\theta}}$ w.r.t. parameters $\boldsymbol{\theta}$ at initialization, \mathcal{K}_{vm} denotes the NTK for VQC-MLPNet, and $\lambda_{\min}(\mathcal{K}_{\text{vm}})$ represents its smallest eigenvalue.

Further decomposing the NTK for the hybrid VQC-MLPNet structure, we have:

$$\mathcal{K}_{\text{vm}} = \mathcal{K}_{\text{vqc}} + \mathcal{K}_{W^{(2)}}, \quad (11)$$

where \mathcal{K}_{vqc} and $\mathcal{K}_{W^{(2)}}$ represent the NTKs for VQC and the classical output layer of MLP, respectively. Because classical neural networks typically possess better-conditioned NTKs [41], integrating the classical components of MLP substantially enhances the smallest eigenvalue, significantly improving trainability relative to standalone VQC:

$$\lambda_{\min}(\mathcal{K}_{\text{vm}}) \gg \lambda_{\min}(\mathcal{K}_{\text{vqc}}). \quad (12)$$

This result confirms the significant improvement in training stability and efficiency offered by VQC-MLPNet compared to standalone VQCs and TTN-VQC.

- **Comparison with MLP and TTN-VQC:**

In summary, compared to classical MLPs, which rely heavily on large-scale parameterization, VQC-MLPNet achieves comparable or superior approximation performance with significantly fewer parameters, thanks to its quantum expressivity. Unlike TTN-VQC, which is constrained by qubit overhead and suffers from optimization difficulties, VQC-MLPNet utilizes classical nonlinear activations to enhance VQC’s stability significantly.

2.3. Empirical Results of Quantum Dot Classification

To support our theoretical findings, we experimentally evaluate the performance of the proposed VQC-MLPNet model on a binary classification task involving charge stability diagrams of single and double quantum dots (QDs). As illustrated in Figure 3, the dataset contains clean (simulated, noiseless) and noisy (practical, noise-contaminated) charge stability diagrams, clearly indicating charge transition lines. Diagrams labeled ‘0’ correspond to single QDs, while those labeled ‘1’ correspond to double QDs. We aim to apply quantum machine learning methods to classify these diagrams based on their characteristic transition line patterns. The experimental evaluation is structured into two distinct settings:

- (i) **Representation Power Assessment:** We first examine the representation power of VQC-MLPNet using clean, noiseless charge stability diagrams. Both training and test data are drawn from the simulated, noise-free environment depicted in Figure 3(a). This setting explicitly evaluates the model’s capability to accurately represent and distinguish the inherent structural differences between single and double QD configurations without interference from external noise.
- (ii) **Generalization Capability Evaluation:** Next, we assess the generalization power of VQC-MLPNet using noisy charge stability diagrams, as shown in Figure 3(b), incorporating realistic noise effects encountered in practical quantum experiments. Here, the model trained on noisy data is tested on unseen noisy diagrams, highlighting its robustness and practical utility in realistic quantum environments.

We conducted comparative experiments to evaluate the representation and generalization capabilities of our proposed VQC-MLPNet, the classical MLP, and the previously developed hybrid TTN-VQC architecture. The primary aims of our experimental setup are as follows:

- To validate that VQC-MLPNet exhibits improved trainability, representation capability, and generalization power relative to MLP and TTN-VQC, consistent with our theoretical analysis.
- To confirm the theoretical predictions regarding the effects of VQC depth and the number of qubits on the performance of the VQC-MLPNet model.

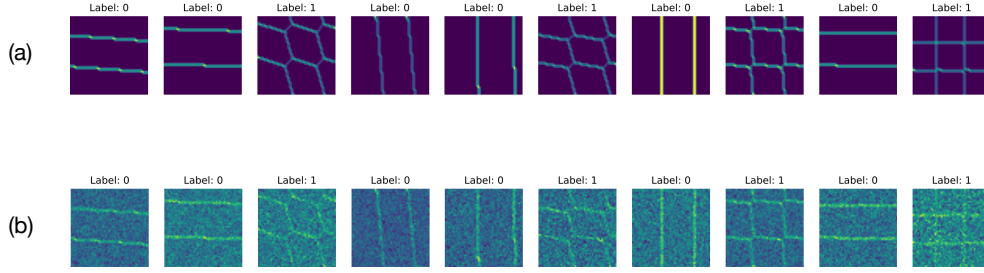


Figure 3. Illustration of single and double quantum dot charge stability diagrams used for classification tasks. (a) Simulated, noise-free charge stability diagrams clearly show charge transition lines. (b) Practical, noise-contaminated stability diagrams reflecting realistic experimental conditions. In both scenarios, Label 0 represents single QD configurations, and Label 1 represents double QD configurations. The quantum machine learning model aims to classify these diagrams by identifying characteristic charge transition line patterns, thereby distinguishing between single-dot and double-dot systems. The simulated noise-free diagrams (a) are employed to evaluate the representation power of the models, while the practical, noisy diagrams (b) assess the models’ generalization capabilities under realistic noise conditions.

- To justify that the quantum-classical VQC-MLPNet architecture is beneficial to the trainability of VQC.
- To verify the practical applicability and effectiveness of the VQC-MLPNet framework in a realistic quantum computing environment.

The experimental dataset comprises 50×50 pixel images representing quantum dot charge stability diagrams, including 2,000 simulated noiseless diagrams and 2,000 diagrams generated under realistic experimental noise conditions. We randomly partition the noiseless diagrams into 1,800 training and 200 test samples to evaluate representation capabilities. Similarly, to assess the models’ generalization capabilities under realistic noise, we utilize 1,800 noisy diagrams for training and reserve 200 noisy diagrams for testing.

In our experiments, the proposed VQC-MLPNet and the baseline TTN-VQC architectures employ VQCs configured with 20 qubits and a circuit depth of 6. All models utilize the cross-entropy loss function, which is optimized through gradient-based parameter updates. For a baseline comparison, we implement an over-parameterized classical MLP with a hidden layer width of 2,048 (explicitly chosen to maintain the over-parameterized and NTK settings), which results in approximately 5.13 million parameters, significantly exceeding the number of training data points. In contrast, our proposed VQC-MLPNet architecture substantially reduces the parameter count to approximately 47.46 thousand parameters, achieving a greater than 100-fold improvement in parameter efficiency due to quantum-enhanced representations.

All models are trained for 20 epochs using the Adam optimizer with a fixed learning rate of 0.001. We employ a fixed random seed across all experiments to ensure reproducibility and fairness, and initialize parameters from a normal distribution.

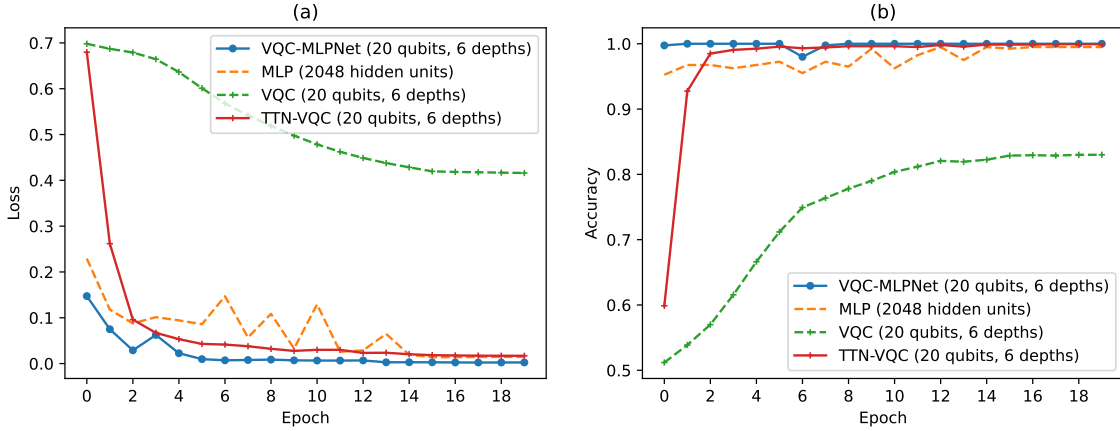


Figure 4. Empirical evaluation of the representation power of VQC-MLPNet compared with classical MLP, standalone VQC, and TTN-VQC. The models are trained and tested using clean (noise-free) quantum dot charge stability diagrams, assessing their ability to approximate and accurately distinguish between single and double quantum-dot configurations. (a) shows training loss, while (b) depicts classification accuracy across training epochs. VQC-MLPNet achieves the fastest convergence, lowest training loss, and highest accuracy, empirically validating its superior representation capability and the theoretical prediction of reduced approximation error compared to alternative models.

Quantum simulations utilize two RTX 4090 GPUs, each equipped with 24 GB of memory.

• Empirical Results on Representation Power:

Figure 4 and Table 2 illustrate the representation capabilities of VQC-MLPNet compared to the classical MLP, standalone VQC, and TTN-VQC architectures evaluated on clean (noiseless) simulated quantum dot charge stability diagrams. The results indicate that VQC-MLPNet consistently achieves the lowest loss (0.00248) and highest accuracy (99.8%) across all epochs, rapidly converging to optimal performance. Although the classical MLP achieves a relatively high accuracy of 99.5%, it exhibits higher training instability, likely due to its substantial parameter count (5.13 million), which is reflected in more noticeable fluctuations during training.

Table 2. Empirical results of QDs classification for the representation power.

Models	Structures	Params.	Loss	Accuracy (%)
VQC-MLPNet	20 Qubits, 6 depths	47.46K	0.00248	99.8 ± 0.06
MLP	2048 hidden units	5.13M	0.01460	99.5 ± 0.04
TTN-VQC	20 Qubits, 6 depths	3283	0.01726	99.6 ± 0.05
VQC	20 Qubits, 6 depths	402	0.41605	83.2 ± 0.10

TTN-VQC shows competitive initial performance, quickly reducing loss and increasing accuracy (99.6%), yet it converges notably slower and exhibits less

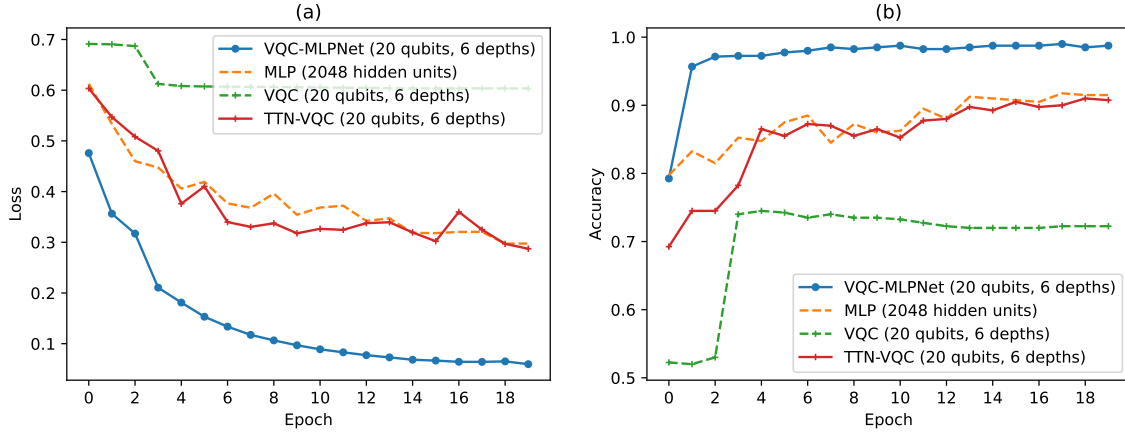


Figure 5. Empirical evaluation of the generalization power of VQC-MLPNet compared with classical MLP, standalone VQC, and TTN-VQC. The training and testing data utilize noisy quantum dot charge stability diagrams that simulate realistic experimental conditions. (a) Training loss and (b) classification accuracy are plotted across epochs. Results demonstrate that VQC-MLPNet achieves the lowest loss, highest accuracy, and quickest convergence, highlighting its superior robustness and improved generalization performance compared to alternative models.

training stability than VQC-MLPNet. The standalone VQC performs poorly overall, achieving the highest loss (0.41605) and lowest accuracy (83.2%), consistent with theoretical predictions of limited representation power due to linearity and optimization difficulties.

These empirical findings strongly support our theoretical analysis by demonstrating that integrating classical nonlinear activations with quantum-generated parameters significantly enhances representation capabilities and effectively reduces approximation error compared to both standalone VQC and TTN-VQC.

• Empirical Results on Generalization Power:

Figure 5 and Table 3 summarize the generalization performance of the evaluated models, tested using noisy quantum dot charge stability diagrams that simulate realistic experimental conditions. The VQC-MLPNet architecture achieves significantly lower test loss (0.0596) and higher accuracy (98.8%) compared to other models, demonstrating its robustness and rapid convergence in realistic noisy scenarios.

In contrast, the classical MLP model shows slower convergence, higher test loss (0.2976), and substantially lower accuracy (91.5%), highlighting its sensitivity to noise-induced data fluctuations. TTN-VQC initially improves quickly but plateaus at a relatively high loss (0.2594) and lower accuracy (90.8%), emphasizing optimization difficulties in fully quantum-based structures. The standalone VQC exhibits severe limitations, reflected by its consistently high loss (0.6034) and significantly reduced accuracy (72.3%), underscoring its limited generalization

Table 3. Empirical results of QDs classification for the generalization power.

Models	Structures	Params.	Loss	Accuracy (%)
VQC-MLPNet	20 Qubits, 6 depths	47.46K	0.0596	98.8 ± 0.06
MLP	2048 hidden units	5.13M	0.2976	91.5 ± 0.06
TTN-VQC	20 Qubits, 6 depths	3283	0.2594	90.8 ± 0.06
VQC	20 Qubits, 6 depths	402	0.6034	72.3 ± 0.08

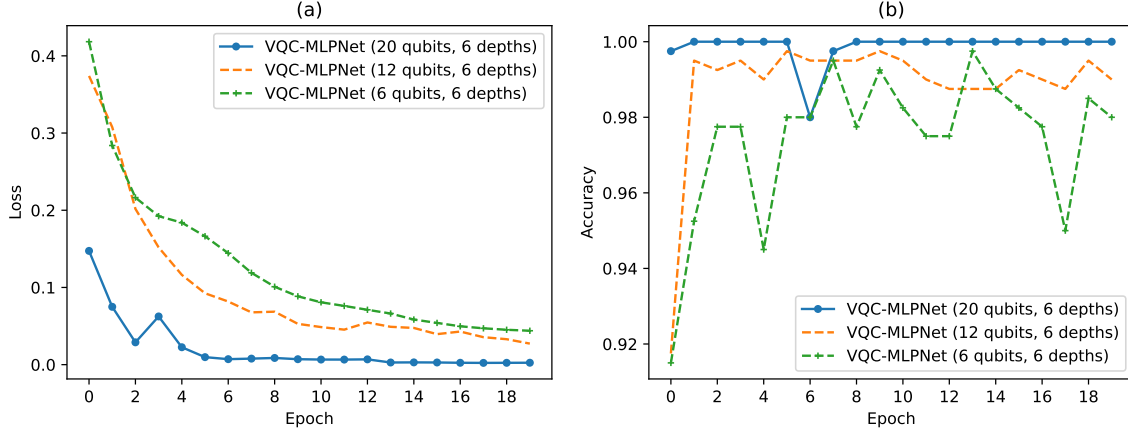


Figure 6. Empirical analysis of how varying the number of qubits affects the representation power of the VQC-MLPNet model, connected to the theoretical approximation error. Clean quantum dot charge stability diagrams are compared for three VQC-MLPNet configurations (with 6, 12, and 20 qubits, at a fixed circuit depth of 6). (a) Training loss and (b) accuracy across epochs indicate that increasing the number of qubits notably enhances representation capability, reduces approximation error, and achieves faster and more stable convergence.

capabilities.

The presented empirical outcomes strongly validate our theoretical predictions, clearly demonstrating that VQC-MLPNet substantially improves generalization power, robustness, and training efficiency compared to purely classical neural networks and existing hybrid quantum-classical architectures under realistic noisy environments.

- **The Effect of Qubit Number on Representation Power:**

Figure 6 illustrates the empirical results assessing how varying the number of qubits influences the representation power of the VQC-MLPNet model, related to our theoretical analysis of the approximation error. Models with different numbers of qubits (6, 12, and 20 qubits), each with a fixed circuit depth of 6, are compared using clean, noiseless quantum dot charge stability diagrams.

From the results in Figure 6, we observe that increasing the number of qubits significantly enhances the model’s representation capability. Specifically, the 20-qubit VQC-MLPNet achieves the lowest training loss and the highest accuracy,

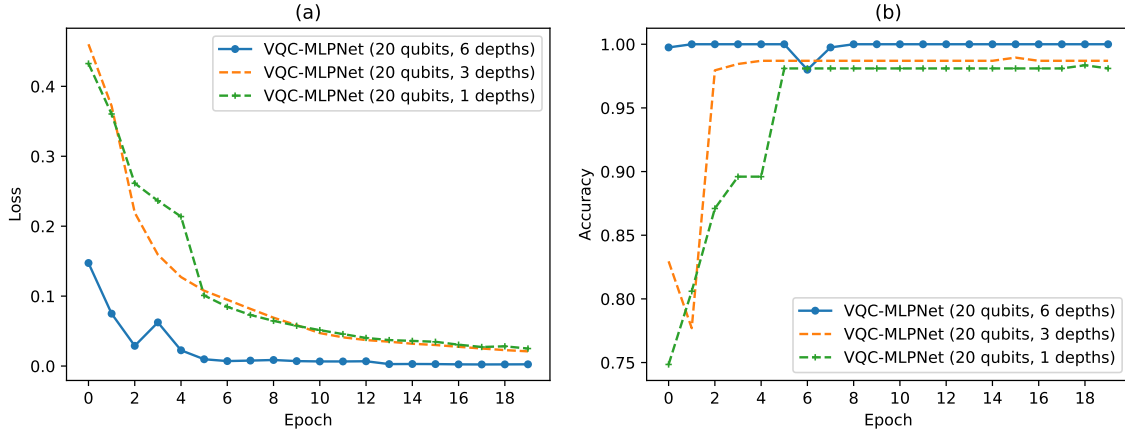


Figure 7. Empirical results demonstrating the impact of varying quantum circuit depths on the representation power of VQC-MLPNet, related to theoretical approximation error analysis. Models with different circuit depths (1, 3, and 6) are evaluated using clean quantum dot charge stability diagrams. (a) Training loss and (b) accuracy curves indicate that deeper circuits significantly improve convergence speed, achieve lower approximation error, and yield higher accuracy, thus enhancing the overall representation capability of the model.

rapidly converging within the initial epochs and maintaining consistently high performance throughout the training process. The 12-qubit model demonstrates competitive performance, yet it shows slightly higher loss and lower accuracy than the 20-qubit model, reflecting a reduction in quantum expressivity. The 6-qubit model displays the slowest convergence, highest loss, and more pronounced fluctuations in accuracy, clearly indicating limited representation power due to insufficient quantum resources.

These experimental observations align closely with our theoretical approximation error analysis, confirming that the approximation power of VQC-MLPNet improves exponentially as the number of qubits increases. This empirically supports our theoretical predictions regarding the critical role of qubit numbers in enhancing the representation capabilities of quantum-enhanced models.

- **The Effect of Quantum Circuit Depth on Representation Power:**

Figure 7 presents empirical results examining how varying the circuit depth of VQC-MLPNet affects its representation power, corresponding to our theoretical approximation error analysis. We compare VQC-MLPNet models with circuit depths of 1, 3, and 6, each utilizing a fixed number of 20 qubits, trained and tested on clean, noiseless quantum dot charge stability diagrams.

As depicted, deeper quantum circuits significantly enhance the representation capacity of the VQC-MLPNet model. The model with the circuit depth 6 achieves the lowest training loss and highest accuracy, quickly converging to nearly perfect performance. In contrast, shallower circuit models (depths 1 and 3) exhibit comparatively higher losses and lower accuracies, converging more slowly and

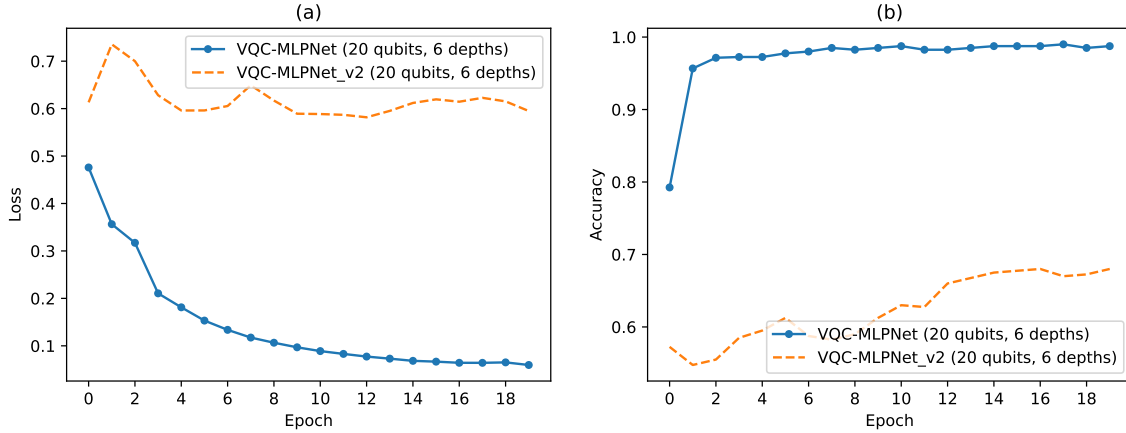


Figure 8. Empirical results comparing optimization performance between the original VQC-MLPNet and the newly proposed VQC-MLPNet_v2 architecture, where two independent VQCs generate the MLP’s weight matrices $W^{(1)}$ and $W^{(2)}$. Both models are configured with 20 qubits and a circuit depth of 6, trained on noisy quantum dot charge stability diagrams. (a) Training loss and (b) accuracy plots demonstrate that the original VQC-MLPNet significantly outperforms VQC-MLPNet_v2, highlighting that the hybrid NTK kernel structure of VQC-MLPNet facilitates better optimization efficiency and stable convergence.

with greater fluctuations, particularly at depth 1. These results demonstrate that increased quantum circuit depth substantially improves the expressivity and representation capability of the model.

These findings empirically validate our theoretical analysis: deeper quantum circuits exponentially reduce approximation error, enabling superior model expressivity and more accurate representation of complex quantum data.

• Optimization Performance Analysis of VQC-MLPNet:

Figure 8 illustrates the empirical results comparing the optimization performance of the original VQC-MLPNet model against a newly proposed structure, VQC-MLPNet_v2, in which two distinct VQCs independently generate weight matrices $W^{(1)}$ and $W^{(2)}$. Both models are configured with 20 qubits and circuit depth 6, trained and evaluated using noisy quantum dot stability diagrams to simulate realistic scenarios.

As Figure 8(a) shows, VQC-MLPNet demonstrates substantially lower training loss, rapidly converging to near-optimal values within a few epochs. In contrast, VQC-MLPNet_v2 exhibits noticeably higher loss and unstable convergence behavior, indicating difficulties in effective optimization. Figure 8(b) further confirms this finding, with VQC-MLPNet quickly achieving and consistently maintaining significantly higher classification accuracy, whereas VQC-MLPNet_v2 struggles to improve and shows limited accuracy throughout training.

These results strongly align with our theoretical optimization analysis based on the NTK. More specifically, the superior performance of VQC-MLPNet empirically

confirms that hybrid architectures, which leverage a balanced combination of quantum and classical kernels, yield a better-conditioned NTK, facilitating efficient optimization and stable convergence. Conversely, the suboptimal performance of VQC-MLPNet_v2 suggests that independently optimized quantum circuits may lead to a less favorable NTK structure, resulting in slower convergence and instability in practical training scenarios.

• Empirical Results Under Realistic IBM Quantum Noises

To further validate the robustness and applicability of the proposed VQC-MLPNet framework in practical quantum computing environments, we simulated realistic noise effects based on the IBM quantum hardware model [42, 43]. We introduced amplitude damping (ADR) and phase damping (PDR) [36] noises at different levels into the quantum circuits of our VQC-MLPNet model during training. The empirical results illustrated in Figure 9 demonstrate that VQC-MLPNet maintains stable and accurate performance despite quantum noise. Even at relatively high noise levels ($\text{ADR} = 0.01$ and $\text{PDR} = 0.01$), the loss curve rapidly converged to low values, and accuracy remained comparable to that in the noise-free scenario, highlighting the architecture’s inherent resilience to quantum hardware imperfections.

This notable robustness arises primarily from the hybrid quantum-classical structure of VQC-MLPNet, where the classical MLP effectively compensates and mitigates quantum noise-induced inaccuracies, preserving overall model stability and predictive power. These findings underscore the practical viability of VQC-MLPNet for quantum machine learning tasks in NISQ devices, reinforcing its potential as a key approach toward achieving quantum advantages in realistic scenarios.

2.4. Empirical Results of Genome TFBS Prediction

Next, we evaluate the proposed VQC-MLPNet’s performance through a genome transcription factor binding sites (TFBS) prediction task. TFBS prediction is a binary classification problem determining whether specific DNA sequences contain particular binding-site patterns. We specifically focus on transcription factor JunD (TF JunD, InterPro entry IPR029823), a crucial activator of the protein-1 family involved in regulating gene transcription across various biological processes.

Our dataset comprises 1,900 genome-wide DNA segments collected from national experiments that identify TF JunD binding sites across all 22 human chromosomes. We partition the dataset into 1,600 segments for training and 300 for testing. Each DNA sequence segment consists of 101 bases labeled according to the presence or absence of the JunD binding site. Each base comprises four nucleotides (A, C, T, or G), so every segment is represented by a 404-dimensional feature vector.

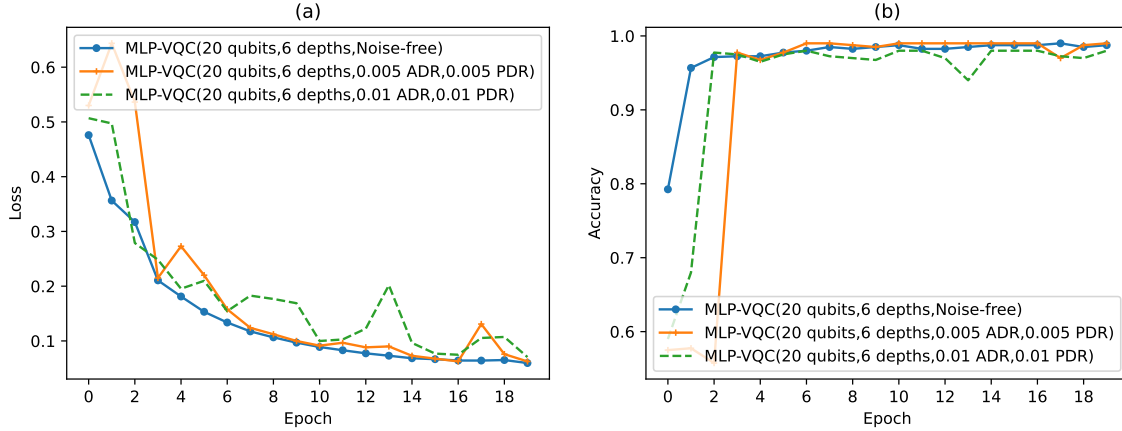


Figure 9. Empirical performance of VQC-MLPNet under realistic IBM quantum noise simulations. (a) Loss curves and (b) accuracy curves of VQC-MLPNet trained on quantum dot classification tasks under noise-free conditions and with varying degrees of IBM quantum noise characterized by amplitude damping rate (ADR) and phase damping rate (PDR). VQC-MLPNet consistently achieves robust performance, exhibiting minimal degradation in accuracy even when exposed to significant quantum noise, highlighting its suitability and resilience for practical quantum computing applications.

We compare the generalization capabilities of the proposed VQC-MLPNet model against standalone VQC, classical MLP, and hybrid TTN-VQC models. Each quantum-based model utilizes 20 qubits and a circuit depth of 6. The classical MLP baseline employs a hidden-layer width of 2,048 units, resulting in approximately 5.13 million parameters, whereas our proposed VQC-MLPNet significantly reduces the parameter count to approximately 47.46 thousand. All models are trained using the cross-entropy loss function optimized with the Adam optimizer and a fixed learning rate of 0.001 for 30 epochs. Identical random seeds and parameter initializations, drawn from a normal distribution, are used to ensure fair comparisons. Quantum simulations are performed using two RTX 4090 GPUs, collectively providing 48 GB of memory.

Figure 10 and Table 4 illustrate the empirical results of our TFBS prediction experiments. Figure 10(a) demonstrates that the VQC-MLPNet achieves significantly lower training loss than classical MLP, TTN-VQC, and standalone VQC, rapidly converging to optimal values. The superior generalization capability of VQC-MLPNet is also evident in Figure 10(b), where it consistently exhibits higher accuracy (93.3%) and more stable convergence across epochs compared to classical MLP (90.5%), TTN-VQC (90.7%), and standalone VQC (68.7%). Notably, the standalone VQC struggles with limited accuracy improvement due to its restricted representation capability, inherent in its linear structure, and optimization challenges. While the classical MLP and TTN-VQC perform better than the standalone VQC, they still exhibit noticeable fluctuations and lower accuracy compared to VQC-MLPNet.

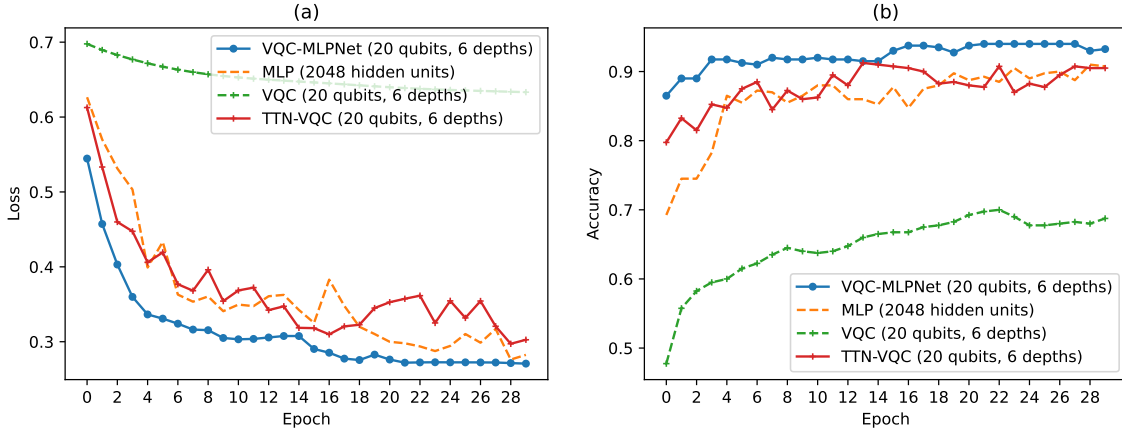


Figure 10. Empirical results for genome TFBS prediction comparing the generalization performance of VQC-MLPNet, classical MLP, standalone VQC, and TTN-VQC. All quantum models employ 20 qubits with a circuit depth of 6, and the classical MLP is configured with 2048 hidden units. (a) Training loss and (b) accuracy demonstrate that VQC-MLPNet achieves significantly faster convergence, lower training loss, and higher accuracy, highlighting its enhanced representation capability and stable optimization compared to other models.

Table 4. Empirical results of the TFBS prediction for the generalization power.

Models	Structures	Params.	Loss	Accuracy (%)
VQC-MLPNet	20 Qubits, 6 depths	47.46K	0.27075	93.3 ± 0.06
MLP	2048 hidden units	5.13M	0.28246	90.5 ± 0.04
TTN-VQC	20 Qubits, 6 depths	3283	0.30262	90.7 ± 0.05
VQC	20 Qubits, 6 depths	402	0.63323	68.7 ± 0.06

Figure 11 further highlights the robustness of VQC-MLPNet under realistic quantum noise conditions simulated using IBM quantum noise with varying ADRs and PDRs. VQC-MLPNet experiences minimal performance degradation compared to the noise-free scenario, maintaining high predictive performance (above 90%) even under increased quantum noise levels. These results validate the inherent resilience and practical applicability of VQC-MLPNet in realistic quantum-enhanced genomic machine-learning scenarios within the NISQ era.

In sum, our empirical findings strongly support our theoretical claims. They demonstrate the enhanced representation power, improved generalization ability, and robustness of VQC-MLPNet, reinforcing its potential as a robust, scalable hybrid quantum-classical architecture for practical genome analysis tasks.

3. Discussion

In this work, we introduce the VQC-MLPNet architecture, a hybrid quantum-classical neural network framework integrating classical MLPs with VQCs, to

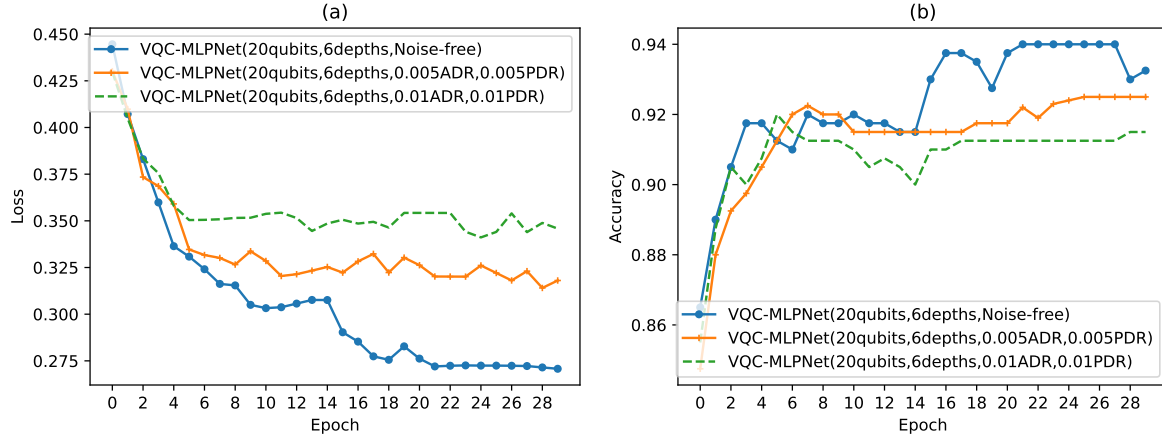


Figure 11. Empirical results for VQC-MLPNet’s performance on genome TFBS prediction under IBM quantum noises. (a) Loss curves and (b) accuracy curves for the VQC-MLPNet model with 20 qubits and 6 depths, comparing noise-free data to varying levels of quantum noise at 0.005 ADR and 0.005 PDR, as well as 0.01 ADR and 0.01 PDR. The results demonstrate the robustness of VQC-MLPNet against different levels of IBM quantum noise, with minimal performance degradation under realistic noise conditions.

address significant limitations in quantum machine learning. Our theoretical analysis rigorously demonstrates that the VQC-MLPNet model systematically enhances approximation capabilities, generalization performance, and optimization stability relative to standalone VQCs and existing hybrid quantum-classical models, such as TTN-VQC. By decomposing the total learning error into approximation, uniform deviation, and optimization components, we derive explicit theoretical upper bounds illustrating the benefits of combining quantum expressivity with classical nonlinear architectures.

Our empirical evaluations substantiate these theoretical predictions, demonstrating that VQC-MLPNet consistently outperforms competing approaches across diverse, challenging tasks, including semiconductor quantum dot classification and genome transcription factor binding site prediction. The experimental results demonstrate the enhanced training efficiency, superior expressivity, and improved generalization capability of the VQC-MLPNet model, particularly under realistic quantum noise conditions representative of near-term quantum computing scenarios.

The success of the VQC-MLPNet approach underscores the importance of effectively integrating classical neural network structures within quantum-enhanced parametric frameworks. This hybrid design paradigm addresses critical barriers in the practical deployment of quantum machine learning algorithms, including optimization instability and limited quantum circuit expressivity. VQC-MLPNet thus represents a significant step toward scalable, reliable, and practical quantum-assisted learning methods, leveraging classical nonlinear activation functions and efficient gradient-based optimization.

We further discuss three critical aspects of our proposed architecture: the rationale

behind choosing the classical MLP as the classical component, the robustness of our model under realistic quantum noise scenarios, and the relevance of VQC-MLPNet to parameter-efficient learning in deep neural networks.

3.1. The Choice of MLP for The Hybrid Quantum-Classical Model

The decision to adopt an MLP as the classical backbone of our hybrid architecture is driven by key practical and theoretical considerations. For one thing, an MLP equipped with a sufficiently large number of neurons can universally approximate complex functions represented by deep neural networks or convolutional neural networks. Thus, the VQC-MLPNet architecture inherits the flexibility and representation power of more sophisticated neural network structures while maintaining a straightforward and computationally efficient form. Furthermore, integrating classical MLPs with quantum circuits significantly enhances the expressivity, trainability, and generalization capabilities of VQCs. These advantages establish the classical MLP as a highly effective choice for boosting VQC performance.

3.2. Practicality and Robustness of VQC-MLPNet Under Realistic Quantum Noise

In evaluating the practical applicability of our proposed VQC-MLPNet architecture, we conducted simulations incorporating realistic IBM quantum noise models [43]. Specifically, we applied amplitude and phase damping channels characterized by their respective damping rates (ADR and PDR) [36]. These quantum noise simulations accurately reflect decoherence mechanisms frequently encountered in real-world quantum computing devices such as superconducting qubit systems. Therefore, our noise modeling provides a reliable assessment of the practical robustness of VQC-MLPNet.

Our experimental results confirm that the VQC-MLPNet model is remarkably robust under these realistic noise conditions. Even at moderate damping levels (e.g., ADR and PDR up to 0.01), VQC-MLPNet maintains excellent classification accuracy and effectively converges during training. This resilience stems from the hybrid architecture, where the classical MLP ensures stable nonlinear processing, while the quantum circuit enhances the model’s expressivity without overexposing it to detrimental quantum noise. Furthermore, the layered structure of VQC-MLPNet partially decouples the classical learning process from quantum noise effects, mitigating the optimization difficulties frequently observed in purely quantum circuits. This robustness significantly enhances the model’s practical utility in contemporary and near-term quantum computing platforms.

3.3. Connection to The Parameter-Efficient Learning of Deep Neural Networks

The VQC-MLPNet architecture significantly contributes to parameter-efficient learning in neural networks [44]. One notable strength of the VQC-MLPNet model is its ability

to retain high expressivity and strong generalization power while drastically reducing the required parameters. Traditional deep neural networks with large hidden layers often suffer from inefficiencies due to the exponentially increasing number of parameters needed to model complex data relationships. Such over-parameterization can lead to training instability, overfitting, and poor generalization, particularly in scenarios with limited data.

In contrast, VQC-MLPNet addresses these issues by incorporating quantum circuits as compact, expressive parameter generators within a classical MLP framework. Quantum circuits inherently offer substantial representational efficiency, enabling the encoding of complex functional relationships in a more compact manner. Consequently, VQC-MLPNet achieves significant reductions in model parameters (e.g., approximately $100\times$ fewer parameters than classical counterparts) without compromising predictive performance. This hybrid approach offers a powerful and general strategy for building efficient deep learning models, achieving the dual objectives of reduced complexity and enhanced generalization capability.

3.4. Comparative Insights into Other Emerging Quantum Architectures

Recent developments in quantum machine learning have introduced several innovative quantum-inspired architectures, such as the Quantum Convolutional Neural Networks (QCNNs) [10] and the Quantum Transformers (QTransformers) [27, 28]. QCNNs utilize quantum convolutional and pooling layers to systematically extract hierarchical features directly within quantum circuits, offering compact parameterizations that are beneficial for structured quantum data, such as quantum states and many-body systems. In contrast, Quantum Transformers utilize attention mechanisms to harness quantum-inspired correlations, thereby effectively capturing long-range dependencies within quantum-enhanced feature spaces. While these models are emerging, they remain primarily quantum-centric, often facing challenges in optimization stability, noise resilience, and generalization on near-term quantum hardware. Our proposed VQC-MLPNet distinctively addresses these limitations by seamlessly integrating quantum circuit expressivity into a classical neural structure, thus improving nonlinear representation capability, optimization stability (as evidenced by favorable NTK properties), and robustness under realistic noise conditions. Consequently, VQC-MLPNet complements existing quantum-centric approaches by providing a practical and scalable hybrid solution suited explicitly for current quantum computing landscapes.

3.5. Potential Broader Impacts of VQC-MLPNet

Beyond the quantum dot classification and genomic prediction tasks demonstrated in this study, the proposed VQC-MLPNet framework holds significant promise for broader scientific domains that require complex, noise-resilient modeling. For instance, the approach could be naturally adapted to computational drug discovery, facilitating quantum-enhanced screening of large molecular datasets. The hybrid architecture's

scalability and robustness against quantum noise in quantum chemistry could also enable more efficient molecular dynamics modeling or predicting electronic structures for complex materials. Furthermore, fields such as climate modeling, where data-driven predictions are challenged by inherent noise and high dimensionality, might benefit from our method’s integration of quantum expressivity and classical nonlinearity.

3.6. Future Work

As illustrated in Figure 1, our current implementation of VQC-MLPNet utilizes amplitude encoding to transform the classical weight matrix $\mathbf{W}^{(1)}$ into quantum states $\left\{|\mathbf{w}_1^{(1)}\rangle, |\mathbf{w}_2^{(1)}\rangle, \dots, |\mathbf{w}_D^{(1)}\rangle\right\}$. The computational complexity of this quantum encoding inherently depends on the dimensionality D of the input data, implying that dimensionality reduction strategies could substantially accelerate the classical-to-quantum encoding process.

In future research, we plan to incorporate a pre-trained tensor network, such as Tensor-Train, to reduce the dimensionality of input data before quantum encoding efficiently. Such tensor networks are well-suited for compressing high-dimensional data while preserving essential quantum correlations and entanglement structures within the data representation. This enhancement is expected to significantly reduce computational overhead during amplitude encoding, thereby improving the scalability and practicality of VQC-MLPNet for larger, real-world quantum machine learning applications.

4. Methods

This section provides methodological support for the theoretical analyses presented in the main text. It introduces the NTK theory, TTN, the TTN-VQC hybrid model, the cross-entropy loss function, and the proof sketches of our derived theoretical results, including the NTK-based analysis of VQC-MLPNet’s trainability. More detailed proofs are presented in the Appendix.

4.1. Introduction to Neural Tangent Kernel Theory

The Neural Tangent Kernel (NTK) is a powerful theoretical tool that explains why deep neural networks can be trained efficiently despite their highly complex structure. At its core, NTK theory examines how small changes in a neural network’s parameters affect its predictions. If slight parameter adjustments consistently lead to stable and predictable changes in output, the network is considered “well-conditioned,” making training smoother and convergence faster.

Formally, the NTK captures this stability by forming a kernel, a similarity measure, that describes the network’s behavior throughout training. A network with a “well-conditioned” NTK, whose smallest eigenvalue is not too small, will have stable gradients during training, enabling efficient optimization via gradient-based algorithms.

Conversely, networks with poorly conditioned NTKs can exhibit instability and slow convergence, commonly referred to as optimization difficulties.

In our work, integrating quantum circuits with classical neural layers (VQC-MLPNet) improves the condition of the NTK, facilitating more efficient training and robust convergence. In particular, while our theoretical analysis builds upon the NTK framework, which formally assumes the infinite-width limit of the MLP component, our practical implementation uses a finite yet sufficiently large hidden width M . Specifically, we set $M = 2048$ in our experiments, a value large enough to closely approximate the NTK regime. Empirical results demonstrate that the model exhibits stable convergence and strong generalization behavior, which is consistent with the theoretical bounds derived under infinite-width assumptions. Thus, NTK theory helps us understand and characterize our model’s training dynamics and provides rigorous guarantees about its performance and generalization capabilities.

4.2. TTN and TTN-VQC

The tensor-train network (TTN) [45], also known as the matrix product state (MPS) [46], is a widely adopted tensor network architecture in machine learning and quantum physics. TTN efficiently represents high-dimensional tensors by factorizing them into a sequence of lower-dimensional tensors, usually matrices or tensors with three indices, arranged in a linear, chain-like structure. When combined with a VQC, TTN forms a hybrid quantum-classical architecture called TTN-VQC. The TTN effectively reduces input dimensionality in this hybrid setup, while the VQC enhances expressivity by introducing quantum-induced nonlinearity. This combination positions TTN-VQC as a robust framework for handling complex, high-dimensional data in quantum machine learning tasks. However, TTN-VQC addresses the common challenges and limitations of hybrid quantum-classical designs, including significant quantum resource requirements, linear representational constraints inherent to quantum circuits, and optimization difficulties due to complex parameter landscapes. Consequently, demonstrating VQC-MLPNet’s superiority over TTN-VQC directly underscores our proposed method’s broader advancements and general applicability within the hybrid quantum-classical modeling paradigm.

4.3. Cross-Entropy Loss Function

The cross-entropy loss function [47] is commonly used in classification tasks, quantifying the discrepancy between predicted probability distributions and the ground-truth labels. It is particularly effective for optimizing probabilistic models, including neural networks and quantum machine learning frameworks. In this study, we utilize the cross-entropy loss with gradient-based optimization methods, guiding model parameters toward improved classification performance by penalizing inaccurate predictions. We consistently apply this loss function to VQC-MLPNet, TTN-VQC, standalone VQC,

and classical MLP models, ensuring a fair and unified assessment of their theoretical convergence and empirical performance.

4.4. Proof Sketch of Theorem 1

Consider a ground truth \mathbf{y} , a target operator h^* , an optimal MLP operator f_{mlp}^* , and an VQC-MLPNet operator $f_{\boldsymbol{\theta}^*}$. The approximation error ϵ_{app} can be upper bounded using the triangle inequality as:

$$\epsilon_{\text{app}} = \mathcal{R}(f_{\boldsymbol{\theta}^*}) - \mathcal{R}(h^*) \leq |\mathcal{R}(f_{\boldsymbol{\theta}^*}) - \mathcal{R}(f_{\text{mlp}}^*)| + |\mathcal{R}(f_{\text{mlp}}^*) - \mathcal{R}(h^*)|. \quad (13)$$

Moreover, the expected risk \mathcal{R} is taken as the cross-entropy loss function such that:

$$|\mathcal{R}(f_{\boldsymbol{\theta}^*}) - \mathcal{R}(f_{\text{mlp}}^*)| + |\mathcal{R}(f_{\text{mlp}}^*) - \mathcal{R}(h^*)| \leq L_{\text{ce}} \|f_{\boldsymbol{\theta}^*} - f_{\text{mlp}}^*\|_2 + L_{\text{ce}} \|f_{\text{mlp}}^* - h^*\|_2, \quad (14)$$

where L_{ce} is a Lipschitz constant induced by the gradient of the cross-entropy loss function with a softmax activation.

As for the first term, we leverage Cybenko's universal approximation theory [48], which leads to

$$\|f_{\boldsymbol{\theta}^*} - f_{\text{mlp}}^*\|_2 \leq \mathcal{O}\left(\frac{1}{\sqrt{M}}\right). \quad (15)$$

Next, we define f_{mlp}^* and $f_{\boldsymbol{\theta}^*}$ operators explicitly:

$$f_{\text{mlp}}^*(\mathbf{x}) = \mathbf{W}^{(2)\top} \sigma(\mathbf{W}_*^{(1)\top} \mathbf{x}), \quad f_{\boldsymbol{\theta}^*}(\mathbf{x}) = \mathbf{W}^{(2)\top} \sigma(\hat{\mathbf{W}}^{(1)\top} \mathbf{x}), \quad (16)$$

and assuming a Lipschitz-continuous activation function $\sigma(\cdot)$, we apply the Cauchy-Swartz inequality, resulting in:

$$\|f_{\boldsymbol{\theta}^*} - f_{\text{mlp}}^*\|_2 \leq \max_{1 \leq j \leq J} \left(\sum_{m=1}^M |\mathbf{w}_m^{(2)}(j)| \right) \|\mathbf{x}\|_2 \left\| \hat{\mathbf{W}}^{(1)} - \mathbf{W}_*^{(1)} \right\|_2. \quad (17)$$

The key term $\left\| \hat{\mathbf{W}}^{(1)} - \mathbf{W}_*^{(1)} \right\|_2$ denotes an induced norm of matrix and can be upper bounded as the sum of encoding error r_{enc} and expressive error r_{exp} :

$$\left\| \hat{\mathbf{W}}^{(1)} - \mathbf{W}_*^{(1)} \right\|_2 \leq \underbrace{\left\| \hat{\mathbf{W}}^{(1)} - \hat{\mathbf{W}}_Q^{(1)} \right\|_2}_{r_{\text{enc}}} + \underbrace{\left\| \hat{\mathbf{W}}_Q^{(1)} - \mathbf{W}_*^{(1)} \right\|_2}_{r_{\text{exp}}}, \quad (18)$$

where $\hat{\mathbf{W}}_Q^{(1)}$ is defined as:

$$\hat{\mathbf{W}}_Q^{(1)} = \left[|\hat{\mathbf{w}}_1^{(1)}\rangle, |\hat{\mathbf{w}}_2^{(1)}\rangle, \dots, |\hat{\mathbf{w}}_D^{(1)}\rangle \right]. \quad (19)$$

On the one hand, the amplitude encoding implies:

$$r_{\text{enc}} \leq \mathcal{O}\left(\frac{1}{2^{\beta U}}\right), \quad (20)$$

with a scaling constant $\beta \in (0, \frac{1}{2})$ and the number of qubits U . On the other hand, since the target matrix W^* is smooth, using the Fourier expansion and exponential decay of coefficients [16, 49], the expressive error satisfies:

$$r_{\text{exp}} \leq \mathcal{O}(e^{-\alpha L}), \quad (21)$$

with circuit depth L and problem-dependent constant $\alpha > 0$. Combining these results yields the approximation error bound as Eq. (7).

4.5. Proof Sketch of Theorem 2

Based on the statistical learning theory, we utilize empirical Rademacher complexity [30, 50] to derive an upper bound for the uniform deviation error ϵ_{dev} :

$$\epsilon_{\text{dev}} \leq 2 \sup_{\boldsymbol{\theta} \in \Theta} \left| \hat{\mathcal{R}}(f_{\boldsymbol{\theta}}) - \mathcal{R}(f_{\boldsymbol{\theta}}) \right| \leq 2\hat{\mathcal{C}}_S(\mathcal{F}_{\text{vm}}), \quad (22)$$

The empirical Rademacher complexity $\hat{\mathcal{C}}_S(\mathcal{F}_{\text{vm}})$ is defined as:

$$\hat{\mathcal{C}}_S(\mathcal{F}_{\text{vm}}) = \frac{1}{|S|} \mathbb{E}_{\boldsymbol{\sigma}} \left[\sup_{\|\mathbf{w}_m^{(2)}\|_1 \leq \Lambda, \|\hat{\mathbf{w}}_m^{(1)}\|_2 \leq \Lambda_Q} \sum_{i=1}^{|S|} \sigma_i \sum_{m=1}^M \mathbf{w}_m^{(2)} \sigma(\hat{\mathbf{w}}_m^{(1)} \cdot \mathbf{x}_i) \right]. \quad (23)$$

Employing techniques of expanding the supremum and bounding used in [24], we obtain:

$$\hat{\mathcal{C}}_S(\mathcal{F}_{\text{vm}}) \leq \frac{\Lambda \Lambda_Q r}{\sqrt{|S|}}, \quad (24)$$

where Λ_Q quantifies quantum circuit complexity and is influenced by circuit depth L . In particular, in line with insights from quantum circuit models and variational quantum algorithms studies [2, 9, 11], we assume that the quantum feature norm Λ_Q scales as $\mathcal{O}(\sqrt{L})$, motivating a refined upper bound as:

$$\hat{\mathcal{C}}_S(\mathcal{F}_{\text{vm}}) \leq \frac{\Lambda \sqrt{L} r}{\sqrt{|S|}}. \quad (25)$$

4.6. The NTK Technique for VQC-MLPNet's Trainability

To analyze the trainability of the VQC-MLPNet model, we consider the operator f_{vm} with a quantum-enhanced weight $\hat{\mathbf{W}}^{(1)} = f_{\text{lin}} \circ f_{\text{vqc}} \circ f_{\text{ae}}(\mathbf{W}^{(1)})$, where f_{vqc} is parameterized by $\boldsymbol{\theta}_{\text{vqc}} = \{\alpha_{1:U}, \beta_{1:U}, \gamma_{1:U}\}$, and the final layer uses classical weights $\boldsymbol{\theta}_{W^{(2)}}$. The VQC-MLPNet operator is given by:

$$f_{\boldsymbol{\theta}}(\mathbf{x}) = \frac{1}{\sqrt{M}} \sum_{m=1}^M \mathbf{w}_m^{(2)} \sigma(\langle \hat{\mathbf{w}}_m^{(1)}, \mathbf{x} \rangle). \quad (26)$$

We define the NTK for VQC-MLPNet, \mathcal{K}_{vm} , as a linear combination of the VQC and the classical weight kernel:

$$\mathcal{K}_{\text{vm}} = \mathcal{K}_{\text{vqc}} + \mathcal{K}_{W^{(2)}}. \quad (27)$$

Since the VQC component of the NTK can be decomposed into contributions from the parameterized quantum gates, for any two data vectors \mathbf{x}_1 and \mathbf{x}_2 , the related NTK $\mathcal{K}_{\text{vqc}}(\mathbf{x}_1, \mathbf{x}_2)$ can be further decomposed as:

$$\mathcal{K}_{\text{vqc}}(\mathbf{x}_1, \mathbf{x}_2) = \mathcal{K}_{\text{vqc}}^{(\alpha)}(\mathbf{x}_1, \mathbf{x}_2) + \mathcal{K}_{\text{vqc}}^{(\beta)}(\mathbf{x}_1, \mathbf{x}_2) + \mathcal{K}_{\text{vqc}}^{(\gamma)}(\mathbf{x}_1, \mathbf{x}_2). \quad (28)$$

Each component is computed over the quantum-enhanced features. For instance, given a constant C_α , the α -parameter NTK contribution is:

$$\mathcal{K}_{\text{vqc}}^{(\alpha)}(\mathbf{x}_1, \mathbf{x}_2) = \frac{1}{M} \sum_{m=1}^M (\mathbf{w}_m^{(2)})^2 \sigma' \left(\langle \hat{\mathbf{w}}_m^{(1)}, \mathbf{x}_1 \rangle \right) \sigma' \left(\langle \hat{\mathbf{w}}_m^{(1)}, \mathbf{x}_2 \rangle \right) \langle \mathbf{x}_1, C_\alpha \mathbf{x}_2 \rangle, \quad (29)$$

with similar expressions for $\mathcal{K}_{\text{vqc}}^{(\beta)}$ and $\mathcal{K}_{\text{vqc}}^{(\gamma)}$ using constants C_β and C_γ as follows:

$$\mathcal{K}_{\text{vqc}}^{(\beta)}(\mathbf{x}_1, \mathbf{x}_2) = \frac{1}{M} \sum_{m=1}^M (\mathbf{w}_m^{(2)})^2 \sigma' \left(\langle \hat{\mathbf{w}}_m^{(1)}, \mathbf{x}_1 \rangle \right) \sigma' \left(\langle \hat{\mathbf{w}}_m^{(1)}, \mathbf{x}_2 \rangle \right) \langle \mathbf{x}_1, C_\beta \mathbf{x}_2 \rangle, \quad (30)$$

$$\mathcal{K}_{\text{vqc}}^{(\gamma)}(\mathbf{x}_1, \mathbf{x}_2) = \frac{1}{M} \sum_{m=1}^M (\mathbf{w}_m^{(2)})^2 \sigma' \left(\langle \hat{\mathbf{w}}_m^{(1)}, \mathbf{x}_1 \rangle \right) \sigma' \left(\langle \hat{\mathbf{w}}_m^{(1)}, \mathbf{x}_2 \rangle \right) \langle \mathbf{x}_1, C_\gamma \mathbf{x}_2 \rangle. \quad (31)$$

Similarly, the classical linear layer NTK is given by:

$$\mathcal{K}_{W^{(2)}}(\mathbf{x}_1, \mathbf{x}_2) = \frac{1}{M} \sum_{m=1}^M \sigma' \left(\langle \hat{\mathbf{w}}_m^{(1)}, \mathbf{x}_1 \rangle \right) \sigma' \left(\langle \hat{\mathbf{w}}_m^{(1)}, \mathbf{x}_2 \rangle \right). \quad (32)$$

In the infinite-width limit $M \rightarrow \infty$, the NTKs converge to their expected values under the initialization distribution. This yields constant kernels for each component (Eqs. (33) and (34)), enabling analytical tractability of convergence behavior.

$$\mathcal{K}_{\text{vqc}}^{(\alpha)}(\mathbf{x}_1, \mathbf{x}_2) \xrightarrow{M \rightarrow \infty} \mathbb{E}_{(\boldsymbol{\theta}_{\text{vqc}}, \boldsymbol{\theta}_{W^{(2)}})} \left[(\mathbf{w}_m^{(2)})^2 \sigma' \left(\langle \hat{\mathbf{w}}_m^{(1)}, \mathbf{x}_1 \rangle \right) \sigma' \left(\langle \hat{\mathbf{w}}_m^{(1)}, \mathbf{x}_2 \rangle \right) \langle \mathbf{x}_1, C_\alpha \mathbf{x}_2 \rangle \right], \quad (33)$$

$$\mathcal{K}_{\text{vqc}}^{(\beta)}(\mathbf{x}_1, \mathbf{x}_2) \xrightarrow{M \rightarrow \infty} \mathbb{E}_{(\boldsymbol{\theta}_{\text{vqc}}, \boldsymbol{\theta}_{W^{(2)}})} \left[(\mathbf{w}_m^{(2)})^2 \sigma' \left(\langle \hat{\mathbf{w}}_m^{(1)}, \mathbf{x}_1 \rangle \right) \sigma' \left(\langle \hat{\mathbf{w}}_m^{(1)}, \mathbf{x}_2 \rangle \right) \langle \mathbf{x}_1, C_\beta \mathbf{x}_2 \rangle \right], \quad (34)$$

$$\mathcal{K}_{\text{vqc}}^{(\gamma)}(\mathbf{x}_1, \mathbf{x}_2) \xrightarrow{M \rightarrow \infty} \mathbb{E}_{(\boldsymbol{\theta}_{\text{vqc}}, \boldsymbol{\theta}_{W^{(2)}})} \left[(\mathbf{w}_m^{(2)})^2 \sigma' \left(\langle \hat{\mathbf{w}}_m^{(1)}, \mathbf{x}_1 \rangle \right) \sigma' \left(\langle \hat{\mathbf{w}}_m^{(1)}, \mathbf{x}_2 \rangle \right) \langle \mathbf{x}_1, C_\gamma \mathbf{x}_2 \rangle \right], \quad (35)$$

$$\mathcal{K}_{W^{(2)}}(\mathbf{x}_1, \mathbf{x}_2) \xrightarrow{M \rightarrow \infty} \mathbb{E}_{\boldsymbol{\theta}_{\text{vqc}}} \left[\sigma' \left(\langle \hat{\mathbf{w}}_m^{(1)}, \mathbf{x}_1 \rangle \right) \sigma' \left(\langle \hat{\mathbf{w}}_m^{(1)}, \mathbf{x}_2 \rangle \right) \right]. \quad (36)$$

Thus, the over-parameterized regime (large-width) ensures the NTK matrix \mathcal{K}_{vm} remains nearly constant throughout training. Furthermore, since classical kernels often

have better-conditioned NTKs [41], introducing the classical component can boost the lowest eigenvalue: $\lambda_{\min}(\mathcal{K}_{\text{vm}}) \gg \lambda_{\min}(\mathcal{K}_{\text{vqc}})$.

Next, we prove the upper bound on the optimization error based on the derived NTK \mathcal{K}_{vm} and $\lambda_{\min}(\mathcal{K}_{\text{vm}})$. Given the set of training data $\{(\mathbf{x}_1, y_1), (\mathbf{x}_2, y_2), \dots, (\mathbf{x}_N, y_N)\}$, we aim to minimize the cross-entropy loss:

$$\hat{\mathcal{R}}(f_{\boldsymbol{\theta}}) = -\frac{1}{N} \sum_{n=1}^N y_n \log(\sigma_c(f_{\boldsymbol{\theta}}(\mathbf{x}_n))), \quad (37)$$

where $\sigma_c(\cdot)$ denotes the softmax probabilities.

Since the parameter update follows gradient flow dynamics:

$$\frac{d\boldsymbol{\theta}}{dt} = -\nabla_{\boldsymbol{\theta}} \hat{\mathcal{R}}(f_{\boldsymbol{\theta}}), \quad (38)$$

we have:

$$\frac{d}{dt} f_{\boldsymbol{\theta}}(\mathbf{X}) = \frac{df_{\boldsymbol{\theta}}}{d\boldsymbol{\theta}} \frac{d\boldsymbol{\theta}}{dt} = -\mathcal{K}_{\text{vm}} \cdot (\sigma_c(f_{\boldsymbol{\theta}}(\mathbf{X})) - \mathbf{y}), \quad (39)$$

where we define the data matrix $\mathbf{X} = [\mathbf{x}_1 \mathbf{x}_2 \dots \mathbf{x}_N]$ and the label vector $\mathbf{y} = [y_1 y_2 \dots y_N]^\top$.

Furthermore, due to the nonlinearity of the activation function $\sigma_c(\cdot)$, we further simplify it by expanding the softmax around the initial predictions. Typically, this linearization approximation is:

$$\sigma_c(f_{\boldsymbol{\theta}_t}(\mathbf{X})) \approx \sigma_c(f_{\boldsymbol{\theta}_0}(\mathbf{X})) + \nabla_{\boldsymbol{\theta}} f_{\boldsymbol{\theta}_0}(\mathbf{X})^\top (f_{\boldsymbol{\theta}_t}(\mathbf{X}) - f_{\boldsymbol{\theta}_0}(\mathbf{X})). \quad (40)$$

Now we have a linear, time-invariant ordinary differential equation (ODE):

$$\frac{d}{dt} f_{\boldsymbol{\theta}_t}(\mathbf{X}) \approx -\mathcal{K}_{\text{vm}} \cdot ([\sigma_c(f_{\boldsymbol{\theta}_0}(\mathbf{X})) - \mathbf{y}] + \nabla_{\boldsymbol{\theta}} f_{\boldsymbol{\theta}_0}(\mathbf{X})^\top (f_{\boldsymbol{\theta}_t}(\mathbf{X}) - f_{\boldsymbol{\theta}_0}(\mathbf{X}))). \quad (41)$$

Solving the above ODE, we obtain a closed form of $f_{\boldsymbol{\theta}_t}(\mathbf{X})$ as:

$$f_{\boldsymbol{\theta}_t}(\mathbf{X}) = f_{\boldsymbol{\theta}_0}(\mathbf{X}) - \nabla_{\boldsymbol{\theta}} f_{\boldsymbol{\theta}_0}(\mathbf{X})^{-1} (I - e^{-\mathcal{K}_{\text{vm}} \cdot \nabla_{\boldsymbol{\theta}} f_{\boldsymbol{\theta}_0}(\mathbf{X})^\top t}) (\sigma_c(f_{\boldsymbol{\theta}_0}(\mathbf{X})) - \mathbf{y}). \quad (42)$$

To minimize $\hat{\mathcal{R}}(f_{\boldsymbol{\theta}_t}(\mathbf{X}))$, we obtain the optimal $\boldsymbol{\theta}^*$ such that

$$f_{\boldsymbol{\theta}^*}(\mathbf{X}) = f_{\boldsymbol{\theta}_\infty}(\mathbf{X}) = f_{\boldsymbol{\theta}_0}(\mathbf{X}) - (\nabla_{\boldsymbol{\theta}} f_{\boldsymbol{\theta}_0}(\mathbf{X}))^{-1} (\sigma_c(f_{\boldsymbol{\theta}_0}(\mathbf{X})) - \mathbf{y}). \quad (43)$$

As for the optimization error ϵ_{opt} , at epoch t , we set $\boldsymbol{\theta}_t = \hat{\boldsymbol{\theta}}$ and further derive that:

$$\begin{aligned} \hat{\mathcal{R}}(f_{\hat{\boldsymbol{\theta}}}) - \hat{\mathcal{R}}(f_{\boldsymbol{\theta}^*}) &\leq L_{\text{ce}} \|f_{\boldsymbol{\theta}_t} - f_{\boldsymbol{\theta}^*}\|_2 \\ &= L_{\text{ce}} \|(\nabla_{\boldsymbol{\theta}} f_{\boldsymbol{\theta}_0}(\mathbf{X}))^{-1} e^{-\mathcal{K}_{\text{vm}} \cdot \nabla_{\boldsymbol{\theta}} f_{\boldsymbol{\theta}_0}(\mathbf{X})^\top t} (\sigma_c(f_{\boldsymbol{\theta}_0}(\mathbf{X})) - \mathbf{y})\|_2 \\ &\leq L_{\text{ce}} \|(\nabla_{\boldsymbol{\theta}} f_{\boldsymbol{\theta}_0}(\mathbf{X}))^{-1}\|_2 \|e^{-\mathcal{K}_{\text{vm}} \cdot \nabla_{\boldsymbol{\theta}} f_{\boldsymbol{\theta}_0}(\mathbf{X})^\top t}\|_2 \|\sigma_c(f_{\boldsymbol{\theta}_0}(\mathbf{X})) - \mathbf{y}\|_2. \end{aligned} \quad (44)$$

Since both \mathcal{K}_{vm} and $\nabla_{\boldsymbol{\theta}} f_{\boldsymbol{\theta}_0}(\mathbf{X})$ are positive semi-definite matrices, using the eigendecomposition techniques, we have:

$$\|(\nabla_{\boldsymbol{\theta}} f_{\boldsymbol{\theta}_0}(\mathbf{X}))^{-1}\|_2 = \frac{1}{\lambda_{\min}(\nabla_{\boldsymbol{\theta}} f_{\boldsymbol{\theta}_0}(\mathbf{X}))}, \quad (45)$$

$$\|e^{-\mathcal{K}_{\text{vm}} \cdot \nabla_{\boldsymbol{\theta}} f_{\boldsymbol{\theta}_0}(\mathbf{X})t}\|_2 = e^{-\lambda_{\min}(\mathcal{K}_{\text{vm}} \cdot \nabla_{\boldsymbol{\theta}} f_{\boldsymbol{\theta}_0}(\mathbf{X}))t}. \quad (46)$$

Thus, we verify the upper bound on the optimization error as:

$$\epsilon_{\text{opt}} = \sup_{\hat{\boldsymbol{\theta}} \in \Theta} \left(\hat{\mathcal{R}}(f_{\hat{\boldsymbol{\theta}}}) - \hat{\mathcal{R}}(f_{\boldsymbol{\theta}^*}) \right) \leq L_{\text{ce}} \cdot \frac{\|\sigma_c(f_{\boldsymbol{\theta}_0}(\mathbf{X})) - \mathbf{y}\|_2}{\lambda_{\min}(\nabla_{\boldsymbol{\theta}} f_{\boldsymbol{\theta}_0}(\mathbf{X}))} \cdot e^{-\lambda_{\min}(\mathcal{K}_{\text{vm}} \cdot \nabla_{\boldsymbol{\theta}} f_{\boldsymbol{\theta}_0}(\mathbf{X}))t}. \quad (47)$$

In practice, since the term $\nabla_{\boldsymbol{\theta}} f_{\boldsymbol{\theta}_0}(\mathbf{X})$ is typically bounded and stable, the primary determinant of convergence rate corresponds to the minimum eigenvalue $\lambda_{\min}(\mathcal{K}_{\text{vm}})$. Thus, we simplify the above term as:

$$\epsilon_{\text{opt}} = \sup_{\hat{\boldsymbol{\theta}} \in \Theta} \left(\hat{\mathcal{R}}(f_{\hat{\boldsymbol{\theta}}}) - \hat{\mathcal{R}}(f_{\boldsymbol{\theta}^*}) \right) \leq C_0 e^{-\lambda_{\min}(\mathcal{K}_{\text{vm}})t}, \quad (48)$$

where the constant $C_0 = \frac{L_{\text{ce}} \cdot \|\sigma_c(f_{\boldsymbol{\theta}_0}(\mathbf{X})) - \mathbf{y}\|_2}{\lambda_{\min}(\nabla_{\boldsymbol{\theta}} f_{\boldsymbol{\theta}_0}(\mathbf{X}))}$.

This analysis shows that the VQC-MLPNet benefits from classical trainability and quantum expressivity. The hybrid NTK structure stabilizes training by providing a favorable eigenvalue spectrum, ensuring effective convergence under practical optimization schemes.

5. DATA AVAILABILITY

The dataset used in our experiments on quantum dot classification can be downloaded from the website: https://gitlab.com/QMAI/mlqe_2023_edx. The dataset for TFBS predictions can be accessed via <https://www.ebi.ac.uk/interpro/entry/InterPro/IPR029823>.

6. CODE AVAILABILITY

Our codes of VQC-MLPNet and other VQC models can be accessed through the website: <https://github.com/jqi41/VQC-MLPNet>.

7. References

- [1] Frank Arute et al., “Quantum Supremacy Using A Programmable Superconducting Processor,” *Nature*, vol. 574, no. 7779, pp. 505–510, 2019.
- [2] John Preskill, “Quantum Computing in the NISQ Era and Beyond,” *Quantum*, vol. 2, pp. 79, 2018.
- [3] Kishor Bharti et al., “Noisy Intermediate-Scale Quantum Algorithms,” *Reviews of Modern Physics*, vol. 94, no. 1, pp. 015004, 2022.
- [4] Frank Leymann and Johanna Barzen, “The Bitter Truth about Gate-based Quantum Algorithms in The NISQ Era,” *Quantum Science and Technology*, vol. 5, no. 4, pp. 044007, 2020.
- [5] M Cerezo, Guillaume Verdon, Hsin-Yuan Huang, Lukasz Cincio, and Patrick J Coles, “Challenges and Opportunities in Quantum Machine Learning,” *Nature Computational Science*, vol. 2, no. 9, pp. 567–576, 2022.
- [6] Jacob Biamonte, Peter Wittek, Nicola Pancotti, Patrick Rebentrost, Nathan Wiebe, and Seth Lloyd, “Quantum Machine Learning,” *Nature*, vol. 549, no. 7671, pp. 195–202, 2017.

- [7] Marcello Benedetti, Erika Lloyd, Stefan Sack, and Mattia Fiorentini, “Parameterized Quantum Circuits As Machine Learning Models,” *Quantum Science and Technology*, vol. 4, no. 4, pp. 043001, 2019.
- [8] Maria Schuld and Nathan Killoran, “Quantum Machine Learning in Feature Hilbert Spaces,” *Physical Review Letters*, vol. 122, no. 4, pp. 040504, 2019.
- [9] Marco Cerezo et al., “Variational Quantum Algorithms,” *Nature Reviews Physics*, vol. 3, no. 9, pp. 625–644, 2021.
- [10] Iris Cong, Soonwon Choi, and Mikhail D Lukin, “Quantum Convolutional Neural Networks,” *Nature Physics*, vol. 15, no. 12, pp. 1273–1278, 2019.
- [11] Amira Abbas, David Sutter, Christa Zoufal, Aurélien Lucchi, Alessio Figalli, and Stefan Woerner, “The Power of Quantum Neural Networks,” *Nature Computational Science*, vol. 1, no. 6, pp. 403–409, 2021.
- [12] Kerstin Beer et al., “Training Deep Quantum Neural Networks,” *Nature Communications*, vol. 11, no. 1, pp. 808, 2020.
- [13] Vojtěch Havlíček et al., “Supervised Learning with Quantum-Enhanced Feature Spaces,” *Nature*, vol. 567, no. 7747, pp. 209–212, 2019.
- [14] Kosuke Mitarai, Makoto Negoro, Masahiro Kitagawa, and Keisuke Fujii, “Quantum Circuit Learning,” *Physical Review A*, vol. 98, no. 3, pp. 032309, 2018.
- [15] Yuxuan Du, Min-Hsiu Hsieh, Tongliang Liu, and Dacheng Tao, “Expressive Power of Parametrized Quantum Circuits,” *Physical Review Research*, vol. 2, no. 3, pp. 033125, 2020.
- [16] Maria Schuld, Ryan Sweke, and Johannes Jakob Meyer, “Effect of Data Encoding on the Expressive Power of Variational Quantum Machine Learning Models,” *Physical Review A*, vol. 103, no. 3, pp. 032430, 2021.
- [17] Hsin-Yuan Huang et al., “Power of Data in Quantum Machine Learning,” *Nature Communications*, vol. 12, no. 1, pp. 1–9, 2021.
- [18] Matthias C Caro et al., “Generalization In Quantum Machine Learning From Few Training Data,” *Nature Communications*, vol. 13, no. 1, pp. 4919, 2022.
- [19] Zoë Holmes, Kunal Sharma, Marco Cerezo, and Patrick J Coles, “Connecting Ansatz Expressibility to Gradient Magnitudes and Barren Plateaus,” *PRX Quantum*, vol. 3, no. 1, pp. 010313, 2022.
- [20] Brian Coyle, Daniel Mills, Vincent Danos, and Elham Kashefi, “The Born Supremacy: Quantum Advantage and Training of An Ising Born Machine,” *npj Quantum Information*, vol. 6, no. 1, pp. 1–11, 2020.
- [21] Yuxuan Du, Min-Hsiu Hsieh, Tongliang Liu, Shan You, and Dacheng Tao, “Learnability of Quantum Neural Networks,” *PRX Quantum*, vol. 2, no. 4, pp. 040337, 2021.
- [22] Jarrod R McClean, Sergio Boixo, Vadim N Smelyanskiy, Ryan Babbush, and Hartmut Neven, “Barren Plateaus in Quantum Neural Network Training Landscapes,” *Nature Communications*, vol. 9, no. 1, pp. 4812, 2018.
- [23] Mohamad H Hassoun, *Fundamentals of Artificial Neural Networks*, MIT press, 1995.
- [24] Jun Qi, Chao-Han Huck Yang, Pin-Yu Chen, and Min-Hsiu Hsieh, “Theoretical Error Performance Analysis for Variational Quantum Circuit Based Functional Regression,” *npj Quantum Information*, vol. 9, no. 1, pp. 4, 2023.
- [25] Samuel Yen-Chi Chen, Tzu-Chieh Wei, Chao Zhang, Haiwang Yu, and Shinjae Yoo, “Quantum Convolutional Neural Networks for High Energy Physics Data Analysis,” *Physical Review Research*, vol. 4, no. 1, pp. 013231, 2022.
- [26] Samuel Yen-Chi Chen, Chih-Min Huang, Chia-Wei Hsing, and Ying-Jer Kao, “An End-to-End Trainable Hybrid Classical-Quantum Classifier,” *Machine Learning: Science and Technology*, vol. 2, no. 4, pp. 045021, 2021.
- [27] Iordanis Kerenidis, Natansh Mathur, Jonas Landman, Martin Strahm, Yun Yvonna Li, et al., “Quantum Vision Transformers,” *Quantum*, vol. 8, pp. 1265, 2024.
- [28] Riccardo Di Sipio, Jia-Hong Huang, Samuel Yen-Chi Chen, Stefano Mangini, and Marcel Worring,

- “The Dawn of Quantum Natural Language Processing,” in *IEEE International Conference on Acoustics, Speech and Signal Processing*, 2022, pp. 8612–8616.
- [29] Francis Bach, *Learning Theory from First Principles*, MIT press, 2024.
- [30] Mehryar Mohri, Afshin Rostamizadeh, and Ameet Talwalkar, *Foundations of Machine Learning*, MIT Press, 2018.
- [31] Junyu Liu, Francesco Tacchino, Jennifer R Glick, Liang Jiang, and Antonio Mezzacapo, “Representation Learning via Quantum Neural Tangent Kernels,” *PRX Quantum*, vol. 3, no. 3, pp. 030323, 2022.
- [32] Arthur Jacot, Franck Gabriel, and Clément Hongler, “Neural Tangent Kernel: Convergence and Generalization in Neural Networks,” *Advances in Neural Information Processing Systems*, vol. 31, 2018.
- [33] Alberto Bietti and Julien Mairal, “On The Inductive Bias of Neural Tangent Kernels,” *Advances in Neural Information Processing Systems*, vol. 32, 2019.
- [34] Hamed Karimi, Julie Nutini, and Mark Schmidt, “Linear Convergence of Gradient and Proximal-Gradient Methods Under the Polyak-Lojasiewicz Condition,” in *Joint European Conference on Machine Learning and Knowledge Discovery in Databases*. Springer, 2016, pp. 795–811.
- [35] Jun Qi, Jun Du, Sabato Marco Siniscalchi, Xiaoli Ma, and Chin-Hui Lee, “Analyzing Upper Bounds on Mean Absolute Errors for Deep Neural Network-Based Vector-to-Vector Regression,” *IEEE Transactions on Signal Processing*, vol. 68, pp. 3411–3422, 2020.
- [36] Kristan Temme, Sergey Bravyi, and Jay M Gambetta, “Error Mitigation for Short-Depth Quantum Circuits,” *Physical Review Letters*, vol. 119, no. 18, pp. 180509, 2017.
- [37] Stefanie Czischek et al., “Miniaturizing Neural Networks for Charge State Autotuning in Quantum Dots,” *Machine Learning: Science and Technology*, vol. 3, no. 1, pp. 015001, 2021.
- [38] Joshua Ziegler et al., “Tuning Arrays with Rays: Physics-informed Tuning of Quantum Dot Charge States,” *Physical Review Applied*, vol. 20, no. 3, pp. 034067, 2023.
- [39] Martin Tompa et al., “Assessing Computational Tools for The Discovery of Transcription Factor Binding Sites,” *Nature Biotechnology*, vol. 23, no. 1, pp. 137–144, 2005.
- [40] Lili Su and Pengkun Yang, “On Learning Over-Parameterized Neural Networks: A Functional Approximation Perspective,” *Advances in Neural Information Processing Systems*, vol. 32, 2019.
- [41] Jaehoon Lee et al., “Wide Neural Networks of Any Depth Evolve As Linear Models under Gradient Descent,” *Advances in Neural Information Processing Systems*, vol. 32, 2019.
- [42] Andrew W Cross, Lev S Bishop, Sarah Sheldon, Paul D Nation, and Jay M Gambetta, “Validating Quantum Computers Using Randomized Model Circuits,” *Physical Review A*, vol. 100, no. 3, pp. 032328, 2019.
- [43] Saloni Resch and Ulya R Karpuzcu, “Benchmarking Quantum Computers and The Impact of Quantum Noise,” *ACM Computing Surveys*, vol. 54, no. 7, pp. 1–35, 2021.
- [44] Chen-Yu Liu, Chao-Han Huck Yang, Hsi-Sheng Goan, and Min-Hsiu Hsieh, “A Quantum Circuit-Based Compression Perspective for Parameter-Efficient Learning,” in *International Conference on Learning Representations*, 2025.
- [45] Ivan V Oseledets, “Tensor-Train Decomposition,” *SIAM Journal on Scientific Computing*, vol. 33, no. 5, pp. 2295–2317, 2011.
- [46] David Perez-Garcia, Frank Verstraete, Michael M Wolf, and J Ignacio Cirac, “Matrix Product State Representations,” *Quantum Information & Computation*, vol. 7, no. 401, 2006.
- [47] Anqi Mao, Mehryar Mohri, and Yutao Zhong, “Cross-Entropy Loss Functions: Theoretical Analysis and Applications,” in *International Conference on Machine Learning*, 2023, pp. 23803–23828.
- [48] George Cybenko, “Approximation by Superpositions of A Sigmoidal Function,” *Mathematics of Control, Signals and Systems*, vol. 2, no. 4, pp. 303–314, 1989.
- [49] Elias M Stein and Rami Shakarchi, *Fourier Analysis: An Introduction*, vol. 1, Princeton University Press, 2011.
- [50] Roman Vershynin, *High-Dimensional Probability: An Introduction with Applications in Data*

Science, vol. 47, Cambridge University Press, 2018.

8. COMPETING INTERESTS

The authors declare no Competing Financial or Non-Financial Interests.